

1 **The Unreasonable Effectiveness of Convolutional Neural Networks in Population**

2 **Genetic Inference**

3

4 Lex Flagel^{1,2}, Yaniv Brandvain², and Daniel R. Schrider^{3,*}

5

6 ¹Monsanto Company, Chesterfield, MO.

7 ²Department of Plant and Microbial Biology, University of Minnesota, St. Paul, MN.

8 ³Department of Genetics, University of North Carolina, Chapel Hill, NC.

9

10 *Corresponding author. Email: drs@unc.edu

11 **ABSTRACT**

12 Population-scale genomic datasets have given researchers incredible amounts of information
13 from which to infer evolutionary histories. Concomitant with this flood of data, theoretical and
14 methodological advances have sought to extract information from genomic sequences to infer
15 demographic events such as population size changes and gene flow among closely related
16 populations/species, construct recombination maps, and uncover loci underlying recent
17 adaptation. To date most methods make use of only one or a few summaries of the input
18 sequences and therefore ignore potentially useful information encoded in the data. The most
19 sophisticated of these approaches involve likelihood calculations, which require theoretical
20 advances for each new problem, and often focus on a single aspect of the data (e.g. only allele
21 frequency information) in the interest of mathematical and computational tractability. Directly
22 interrogating the entirety of the input sequence data in a likelihood-free manner would thus offer
23 a fruitful alternative. Here we accomplish this by representing DNA sequence alignments as
24 images and using a class of deep learning methods called convolutional neural networks (CNNs)
25 to make population genetic inferences from these images. We apply CNNs to a number of
26 evolutionary questions and find that they frequently match or exceed the accuracy of current
27 methods. Importantly, we show that CNNs perform accurate evolutionary model selection and
28 parameter estimation, even on problems that have not received detailed theoretical treatments.
29 Thus, when applied to population genetic alignments, CNN are capable of outperforming
30 expert-derived statistical methods, and offer a new path forward in cases where no likelihood
31 approach exists.

32 INTRODUCTION

33 Using genetic data to make inferences about the natural histories of populations represents a
34 major goal of evolutionary research. As the ever-increasing throughput of DNA sequencing
35 technologies makes the generation of large population genomic data sets more routine,
36 researchers can leverage patterns of genetic variation across the genome to characterize the
37 evolutionary forces at play (Hahn 2018). For example, advances have been made in identifying
38 historical demographic events such as population size changes (Marth *et al.* 2004; Tennessen *et al.*
39 2012; Gazave *et al.* 2014) and genetic exchange between populations and species (Martin *et al.*
40 2013; Hellenthal *et al.* 2014; Sankararaman *et al.* 2014; Corbett-Detig and Nielsen 2017; Schrider
41 *et al.* 2018). Population genomic analyses have also revealed the pervasive impact of selection on
42 linked neutral polymorphism (Begun and Aquadro 1992; Begun *et al.* 2007; Langley *et al.* 2012;
43 Elyashiv *et al.* 2016), both through positive selection (Maynard Smith and Haigh 1974; Kaplan *et al.*
44 1989) and purifying selection (Charlesworth *et al.* 1993). As the volume of population genomic
45 data sets has increased, so too has the demand for powerful computational methods capable of
46 using these data to learn about the fundamental evolutionary processes shaping genomic
47 variation.

48 To meet this need, myriad statistical and computational tools have been devised to
49 answer evolutionary questions using population genetic data. One particularly common
50 paradigm, which predates the high-throughput sequencing revolution, is that of the population
51 genetic summary statistic: a value (or sometimes a vector of values) designed to capture the
52 information present in a sequence alignment of individuals from one or more populations. When
53 a particular evolutionary phenomenon acts on a population it alters the shapes of genealogies,
54 and this effect is manifest in the observed sequence alignment. For example, a population
55 expansion will result in genealogies with longer branches near the leaves of the tree, which will
56 manifest as an excess of rare alleles. Many summary statistics seek to uncover the signature of
57 these genealogical skews through their effect on the alignment; e.g. Tajima's D will be negative
58 following a recent expansion or recovery from a bottleneck (Tajima 1989; Simonsen *et al.* 1995).
59 Ideally a summary statistic will only detect the signal of the evolutionary process it is being used
60 to investigate, but in practice summary statistics are frequently confounded by other forces that
61 may have similar effects on the shapes and/or sizes of genealogies. For example, Tajima's D is
62 sensitive to positive selection as well as population size changes (Simonsen *et al.* 1995). Moreover,

63 such summary statistics do not capture all of the information present in the alignment. Thus a
64 major challenge of population genetic inference is to create methods that utilize as much
65 information from the input data as possible in order to maximize our ability to distinguish among
66 the numerous evolutionary processes that can give rise to an observed signal.

67 One approach researchers have adopted to address this challenge is to incorporate a
68 larger number of observations from the data into likelihood-based inference methods. However,
69 calculating likelihoods of population genomic data sets is often mathematically and
70 computationally intractable, and therefore such approaches often use composite likelihoods
71 which ignore the non-independence of observations (e.g. Hudson 2001; Nielsen *et al.* 2005). For
72 example, Nielsen *et al.*'s SweepFinder (2005), which examines allele frequencies at
73 polymorphisms flanking a focal region to determine whether that region has experienced a recent
74 selective sweep (Maynard Smith and Haigh 1974), treats each allele frequency as an independent
75 observation despite the partially shared evolutionary histories linked alleles experience. Another
76 drawback of most likelihood-based methods is that they generally compute the likelihood of only
77 a few features of the data (often only one), and therefore additional information that could
78 improve accuracy is ignored. For example, SweepFinder examines allele frequencies but ignores
79 linkage disequilibrium (LD), which is elevated in areas flanking the selected site (Kim and Nielsen
80 2004). Hidden Markov models (Hobolth *et al.* 2007; Boitard *et al.* 2009; Dutheil *et al.* 2009; Kern
81 and Haussler 2010), including those based on the sequential Markov coalescent (Li and Durbin
82 2011; Schiffels and Durbin 2014), have also proved effective at using population genetic
83 observations along a recombining chromosome to make evolutionary inferences.

84 More recently, population geneticists have begun to explore an alternative strategy of
85 using a large set of complementary summary statistics for model selection and parameter
86 estimation, an approach that often results in more powerful and robust inference (e.g. Lin *et al.*
87 2011; Pybus *et al.* 2015; Gao *et al.* 2016; Schrider and Kern 2016; Sheehan and Song 2016). Each
88 summary statistic seeks to measure a particular attribute of the genealogy, and one can thus
89 design a customized set of summary statistics to more fully represent the genealogical information
90 present in the sequence alignment. This view deploys summary statistics less for their individual
91 links to underlying theory, and more for their collective ability to perform pattern recognition.
92 The challenge then becomes extracting information about the underlying evolutionary processes
93 from the set of summary statistics. Two exciting approaches for dealing with this challenge that

94 have garnered increasing attention in recent years are approximate Bayesian computation (ABC;
95 reviewed in Beaumont 2010) and supervised machine learning (reviewed in Schrider and Kern
96 2018). Both of these approaches make use of suites of user-defined summary statistics and
97 training data generated under known parameters to identify reasonable evolutionary models and
98 parameterizations that could have generated the observed data. Here we focus on the supervised
99 machine learning approach, as it sets the scene for the convolutional neural networks described
100 below.

101 In the terminology of supervised machine learning, each summary statistic is called a
102 feature, and the full set of statistics used is called a feature vector. To use supervised machine
103 learning, a researcher must first obtain training data (often referred to as “labeled” data)—a set of
104 data points each summarized by a feature vector (the explanatory variables) accompanied by a
105 known outcome (the response variable). Next, a supervised machine learning algorithm is trained
106 to predict the outcome given the feature vector using the labeled training data. Thus, the
107 supervised machine learning technique automates the process of extracting information and
108 constructing rules from a set of summary statistics. Across many areas of research, supervised
109 machine learning techniques are fast replacing rules developed by human experts because they
110 are often more accurate (LeCun *et al.* 2015).

111 Supervised machine learning methods are increasingly being applied to numerous
112 problems in population genetics (Schrider and Kern 2018). In this context, labeled training data
113 are usually generated via population genetic simulation, an endeavor that has grown
114 considerably more feasible given recent improvements in simulation flexibility and efficiency (e.g.
115 Thornton 2014; Kelleher *et al.* 2016; Haller and Messer 2017; Kelleher *et al.* 2018). To date,
116 population genetic applications of machine learning include demographic inference (Pudlo *et al.*
117 2016; Sheehan and Song 2016), local ancestry inference (Schrider *et al.* 2018), inferring
118 recombination rates (Lin *et al.* 2013; Gao *et al.* 2016), and detecting genomic regions experiencing
119 recent selective sweeps (Pavlidis *et al.* 2010; Lin *et al.* 2011; Ronen *et al.* 2013; Pybus *et al.* 2015;
120 Schrider and Kern 2016). While such methods have great promise, they still rely on a user-
121 defined set of summary statistics (ranging in number from dozens to hundreds). Moreover, it is
122 not known whether it is possible to construct a set of statistics that sufficiently captures all
123 relevant information in the input data.

124 Unlike other machine learning approaches, convolutional neural networks (CNN; LeCun
125 *et al.* 1998) are pattern recognition algorithms that do not require a predefined feature vector.
126 When fed labeled training data (e.g. a set of haplotypes simulated under a known biological
127 scenario), a CNN discovers meaningful features, in essence making a feature vector, and then
128 extracts information from these features in order to make inferences. CNNs have proved effective
129 in a number of fields (reviewed in LeCun *et al.* 2015), and particularly in the field of image
130 recognition, where they have achieved dramatic improvements over previous efforts (e.g.
131 Lawrence *et al.* 1997; Krizhevsky *et al.* 2012; Simonyan and Zisserman 2014). The application of
132 CNNs to population genomic inference is just beginning, and shows great promise (Chan *et al.*
133 2018). Population genetic questions may be particularly well suited for CNN-based learning
134 because they take matrices as inputs, and alignments of sequenced chromosomes are quite
135 naturally represented in this manner.

136 The goal of this paper is to assess the effectiveness of CNNs as a general strategy for
137 population genomic inference. We demonstrate that CNNs can be successfully applied to a
138 number of population genomic problems, in some cases achieving surprising accuracy. In
139 particular, we use simulation to show that CNNs can leverage images of aligned sequences to
140 accurately uncover regions experiencing gene flow between related populations/species, estimate
141 recombination rates, detect selective sweeps, and make demographic inferences. Indeed, in most
142 cases we observe performance that matches or exceeds that of current methods. We also use a
143 CNN to accurately infer recombination rates from read coverage data in a simulated
144 autotetraploid, demonstrating this approach's flexibility in handling noisy data while solving a
145 complex problem for which no theoretical solution exists. In light of these encouraging findings,
146 we argue that population genetics researchers should consider CNNs as a potential solution to a
147 variety of problems involving evolutionary inferences from sequence data. Because some readers
148 may have little background with this tool, we also provide an overview of the inner workings of
149 CNNs and explore several technical considerations that may impact performance.

150

151 **RESULTS**

152 Our goal is to use a CNN to make population genetic inferences from an alignment image, which
153 can be thought of as matrices where each entry represents the allele present in a given
154 chromosome at a given site. In particular, we focus on four distinct problems: identifying local

155 introgression, estimating the recombination rate, detecting selective sweeps, and inferring
156 population size changes. We chose these four tasks because each represents a different challenge
157 in population genetic inference, each with its own attendant branch of theory. To show the
158 ability of CNNs to solve problems for which no statistical approaches have been proposed, we
159 extended our recombination inference to infer recombination rates in autotetraploids with
160 tetrasomic inheritance.

161 Below, we address each of these problems in turn, providing a brief overview of the
162 phenomenon in question and existing methodology before describing our results using CNNs.
163 But prior to tackling these problems, we first give an overview of CNNs and discuss strategies for
164 reorganizing our input data that we found helpful in making CNNs work more efficiently with
165 population genetic alignments.

166

167 **Overview of convolutional neural networks**

168 Internally, a CNN is a type of artificial neural network – a collection of connected layers of
169 combinatorially linked mathematical functions (termed *artificial neurons*) that take an input and
170 transform it into an output value (Mitchell 1997). In a typical fully connected artificial neural
171 network, the input values are fed through a series of layers of artificial neurons (fig. 1A), termed
172 hidden layers, before reaching the output layer which transforms its inputs into a final prediction.
173 The output for the j^{th} neuron within one of the hidden layers is given by the following:

$$f\left(\sum_i^n w_{ij}x_i + b_j\right)$$

174 In the expression above, x_i is the neuron's i^{th} input value (either an input value from the data or
175 from a neuron in the previous layer's output), and w_{ij} is the *weight* attached to the connection
176 between that node (i) and the current node (j) and b_j is the current node's *bias* term. That is, to
177 obtain the value of neuron j , we compute the linear combination of the vector containing all
178 values from the previous layer and the j^{th} neuron's vector of weights; the results of this summation
179 are in turn added to neuron j 's bias term and then fed as input to some function f , termed the
180 *activation function* and which may be nonlinear. Thus, an artificial neural network is a
181 mathematical function.

182 Importantly, by changing the values of the weights and biases, an artificial neural network
183 can be tuned to detect informative patterns in the input data in order to produce the desired

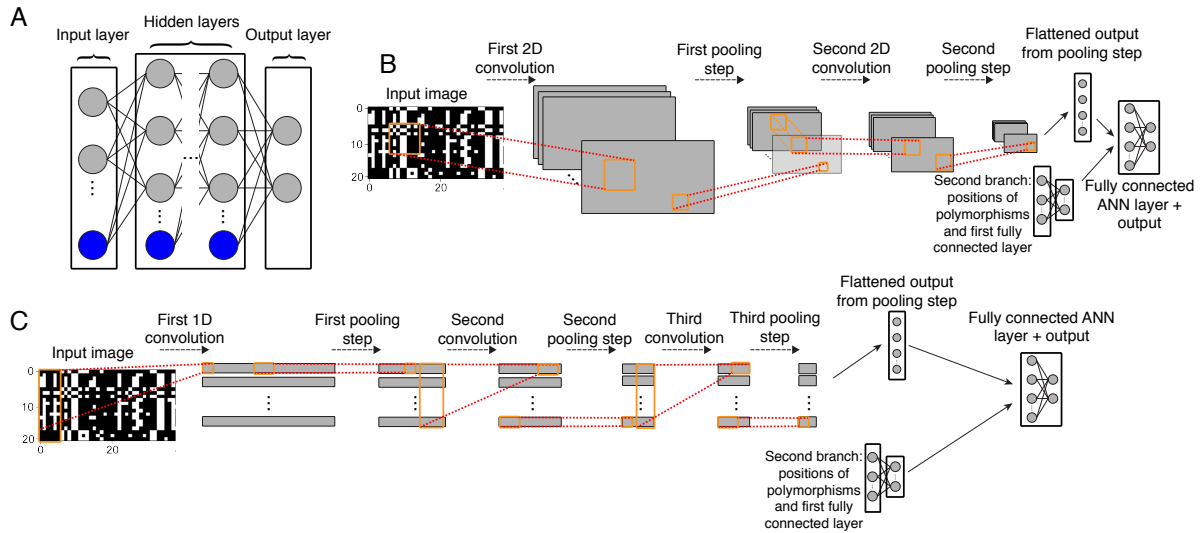


Fig. 1: Schematics of a standard feedforward neural network and two convolutional neural network designs used in this study. A) Diagram of a fully connected feedforward neural network. Gray circles represent input (left side), output (right side), or hidden (center) neurons. Blue circles represent collections of bias terms. With the exception of the input layer, the value of any given neuron is a linear combination of values from the previous layer plus a bias term; this sum is then passed to an activation function (not shown). Each edge represents a distinct weighted input or bias term. Outputs may represent class membership posterior probabilities or estimates of continuous variables. B) A diagram of a 2D CNN similar to that used in this study to infer demographic parameters. The input is an alignment represented as an image which is passed through a first convolutional layer in order to create a set of feature maps. These feature maps are then downsized via a pooling step which replaces the values of a 1 or 2D matrix within a feature map with a single value summarizing it (e.g. the mean or maximum value of that matrix). For example, a 2D pooling operation of size 2 will reduce the size of a feature map by a factor of 4, as each adjacent 2×2 matrix within the input feature map is replaced by a single value (e.g. the maximum of those four values). These downsized feature maps are then passed through a second convolutional filter and pooling step, and the resulting output is flattened into a one dimensional vector and passed as input into a fully connected feedforward layer (bias terms not shown). Also passed into this layer is output from a second branch of this network: the vector of positions of segregating sites in the alignment which have been passed through their own fully connected layer. Finally, the last fully connected neural network layer yields the predicted output values. C) Similar to panel B, but showing a 1D CNN with three convolutional layers (each followed by a pooling step), as used for our recombination rate estimator.

184
185 output. In the case of image recognition, an image is first represented numerically, typically as a
186 matrix of pixel intensities, and then transformed by the artificial neural network to produce an
187 output, for example a prediction of the type of object in the image. CNNs (Fig. 1B–C) differ from

188 standard artificial neural networks in that they begin with one or more convolutional layers, in
189 which a series of smaller weight matrices referred to as “filters” slide across the input image—
190 mimicking the manner in which animal cortical neurons each focus on input only from a small
191 receptive field—and perform a matrix convolution at each step until a series of filtered image
192 matrices are produced (LeCun *et al.* 1998). These filters are constructed during training (see
193 below). Each convolutional layer is often followed by a pooling layer (see Fig 1B and caption)
194 which reduces the size of these filtered image matrices while maintaining potentially important
195 discriminatory information obtained by the convolutional filters. Finally, these matrices are
196 flattened into one-dimensional vectors and then fed into a fully connected (or “dense”) artificial
197 neural network (for an accessible overview see LeCun *et al.* 2015). Thus, salient features derived
198 from the image matrix by the convolutional and pooling layers are passed into one or more
199 layers of a fully connected neural network whose output layer then yields our predicted response
200 value.

201 CNNs allow for two types of convolutional layers: 1-dimensional and 2-dimensional,
202 which differ only with respect to the possible shapes that the convolutional filter can take (Fig.
203 1B–C). 1-dimensional (1D) convolutions are often used in the application to time-series data (e.g.
204 Dieleman and Schrauwen 2014; Kim 2014), and are thus applicable to sequence alignment
205 matrices. Despite its name, a 1D filter is not a vector but rather a rectangular matrix that spans a
206 user-defined number of entries (called the “kernel size”) in one dimension in the input data (in
207 our case this dimension is that of the polymorphic sites in the alignment), and stretches entirely
208 across the other dimension (in our case across all chromosomes in the sample). A 2-dimensional
209 (2D) convolutional filter, which is more often used with image data, allows the user to specify
210 both dimensions of the filter matrix (often using a square matrix). Whether 1- or 2-dimensional,
211 the benefit of incorporating convolutions is that it allows the CNN to take advantage of structural
212 information in the input data. For example, from an image of a face, a CNN can learn to detect
213 the repeated pattern of the eye shape and the location of both eyes relative to one another and to
214 other features. When there is meaningful structural information such as this, CNNs tend to
215 outperform non-convolutional neural networks.

216 Here our input data is an alignment of linked segregating sites with partially shared
217 evolutionary histories. Our hope is that a CNN can discover structural information in these data
218 in order to make evolutionary inferences—for example, locating the valley in diversity at the

219 center of a sweep (Maynard Smith and Haigh 1974), the “shoulders” on the flanks of a sweep
220 where linkage disequilibrium and allele frequencies are both elevated (Schridder *et al.* 2015), or
221 even the spatial relationship between these patterns. We also note that neural networks such as
222 CNNs can have multiple “branches” each with separate architectures and input types—in some
223 of the cases discussed in this paper we incorporate an additional network branch whose input is
224 the vector of the positions of the segregating sites (Fig. 1B–C).

225 Like all supervised machine learning methods, a CNN must be trained on labeled
226 training data before it can make predictions on unlabeled data (i.e. data whose response variables
227 are unknown). Training is accomplished by tuning the weights and biases that control the
228 behavior of its artificial neurons so that together they maximize the accuracy of the outputs on
229 the training data. Note that the weights determined during the training process include the values
230 of the convolutional filter matrices, and thus different filters will be algorithmically created for
231 each task we address in this paper. This tuning occurs over a number of iterations using the
232 backpropagation algorithm (Rumelhart *et al.* 1986), which in modern implementations feeds a
233 small number of training examples (a “mini-batch”) through the network and then estimates the
234 error gradient on the output vectors produced for these examples. The error gradient is then
235 propagated in reverse through the network—a given hidden neuron’s contribution to the error is
236 proportional to the linear combination of its weight vector and the errors associated with each
237 neuron in the next layer. The weights are then updated using one of the many flavors of
238 stochastic gradient descent (e.g. Kingma and Ba 2014). This process repeats until each training
239 example has been fed through the network, marking the completion of a single training iteration.
240 Training continues for a number of these iterations (often called epochs) until a specified stopping
241 criterion is reached (e.g. a predefined number of iterations has been performed, accuracy on the
242 validation set has not improved relative to the previous iteration, etc.).

243 In the context of population genetics, the CNN’s input could be a matrix of allelic states
244 at each polymorphic site (Fig. 2). For example, an alignment of haploid individuals M , where
245 $M_{ij}=0$ if the i^{th} individual has the ancestral allele at the j^{th} segregating site in the alignment, and 1
246 if this individual has the derived allele (an input format that can easily be altered to allow for
247 multiallelic polymorphisms); we adopt this approach and variants of it below. The output can be
248 a categorical indicator (e.g. whether or not the genomic window experienced a recent selective
249 sweep) in which the problem is referred to as a classification task in machine learning

250 terminology, a quantitative value (e.g. the population recombination rate) in which case the task
251 is referred to as regression, or a vector containing both categorical and quantitative values. Once
252 the CNN has been trained to produce the desired output, it can be applied to unlabeled data (e.g.
253 sequence from natural populations).
254

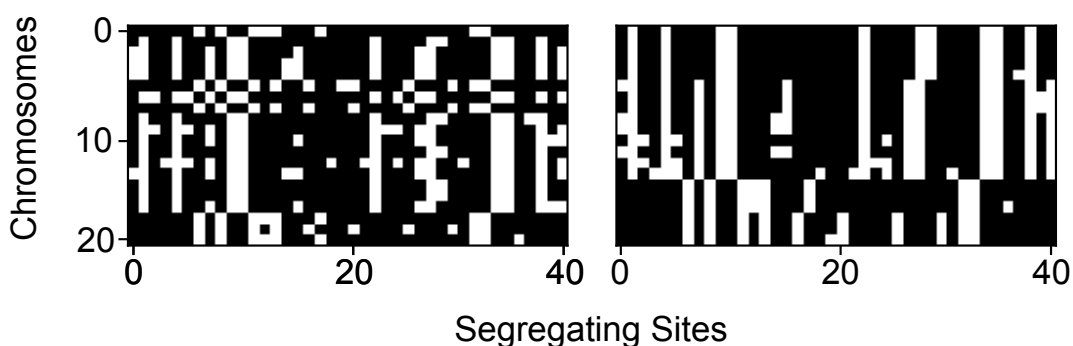


Fig. 2: Example population genetic alignments visualized as black-and-white images. An unsorted alignment matrix (left) and this same matrix sorted by genetic similarity among chromosomes (right) are shown. Each row represents one of twenty chromosomes in the sample and each column represents one of forty segregating sites. Derived and ancestral states are encoded as black and white, respectively.

255
256 Because supervised machine learning relies on predictive functions tuned algorithmically
257 from training data, CNNs can be applied to any problem for which a training set can be
258 obtained, and therefore our inference is not limited to problems for which appropriate likelihood
259 models or statistics have been derived and implemented. In a population genetics context,
260 coalescent simulations provide a versatile and computationally efficient (Hudson 2002; Teshima
261 and Innan 2009; Ewing and Hermisson 2010; Kelleher *et al.* 2016; Kern and Schrider 2016)
262 means to generate training data. In this paper we relied exclusively on coalescent simulations to
263 produce training data for the CNN. However, compute-intensive forward population simulations
264 may offer greater flexibility than coalescent simulations in some situations, and recent advances
265 are making them more computationally feasible (Kelleher *et al.* 2018).

266 267 **Using a CNN to make inferences from an alignment: a simple test case**

268 We evaluated the performance impact of transposing the alignment matrix (so that columns
269 rather than rows correspond to chromosomes) and sorting the chromosomes in the alignment
270 matrix by genetic similarity. We did this using a 1D CNN trained to estimate the population-

271 scaled mutation rate, θ , in an equilibrium population. We found that both of these techniques
272 accelerate the decline in root-mean-square error (RMSE; Fig. 3), showing that they help the
273 network achieve better performance. Transposing the alignment matrix so that chromosomes are
274 represented by rows and polymorphisms by columns has a particularly notable effect (compare
275 blue and black lines in Fig. 3). Additionally, sorting the chromosomes by genetic similarity further
276 increases the accuracy of the CNN when combined with the matrix transposition above
277 (magenta line); alternatively, using a permutation-invariant network architecture would obviate
278 any need for this step (Chan *et al.* 2018). The effect of transposition should disappear when using
279 2D convolutions because in those cases we always used a square convolutional filter matrix
280 (Methods), but we found that 1D CNNs often performed as well as 2D CNNs (data not shown).
281 Thus, unless otherwise specified we use 1D convolutions for the tasks discussed below.
282

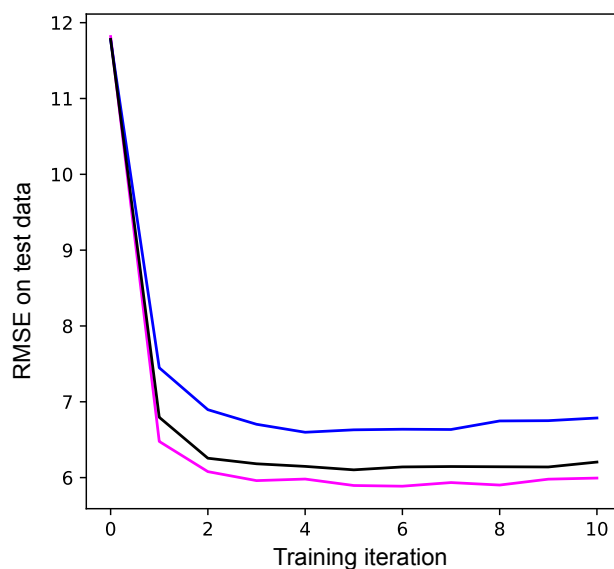


Fig. 3: The impact of input data reorganization on accuracy. We show the root mean squared error (RMSE) of a 1D CNN's predictions of θ as assessed on 1,000 test alignments after a given number of training iterations. Each line is the average of 10 runs. The blue line shows accuracy after training using alignment matrices with each row representing one chromosome. The black line shows accuracy after transposing all matrices so that chromosomes correspond to columns; this makes 1D convolutional filters examine each individual at a group of adjacent segregating sites. The magenta line shows the impact of transposing matrices, and sorting the chromosomes in the alignment matrix by genetic similarity.

283
284

CNN's can accurately detect introgressed loci

285 Recent studies indicate that closely related species often exchange genes (Kulathinal *et al.* 2009;
286 Martin *et al.* 2013; Brandvain *et al.* 2014; Fontaine *et al.* 2015). There are several motivations for
287 locating genomic segments introgressed from one species into another. For one, the occurrence
288 of cross-species gene flow raises the possibility of adaptive introgression, wherein a beneficial
289 allele enters a population via migration from a related species (reviewed in Hedrick 2013).
290 Discovering introgressed loci can therefore identify alleles underlying rapid ecological adaptation
291 as well as the source of these alleles. In addition, uncovering genomic regions that are and are not
292 porous to cross species gene flow may help to illuminate the genomic basis of reproductive
293 isolation (Turner *et al.* 2005).

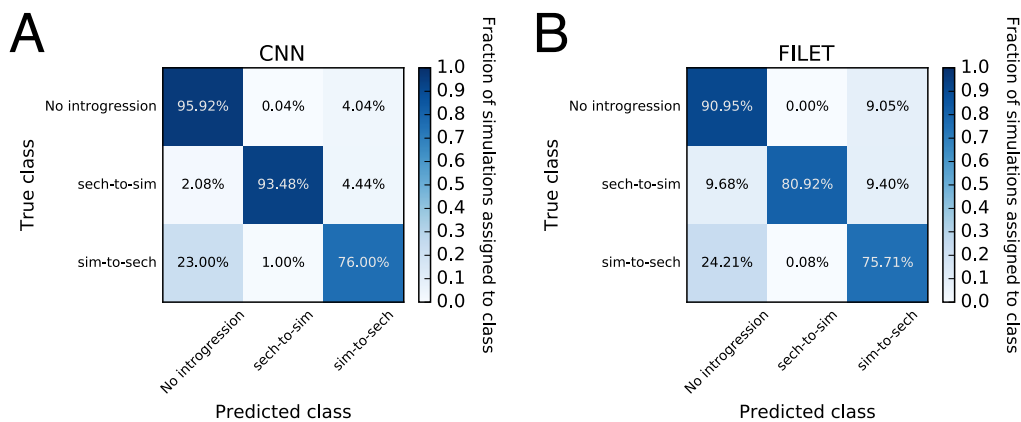


Fig. 4: Performance of classifiers for detecting introgression. We use confusion matrices to show the performance of a CNN trained to detect genomic regions of introgression between two closely related species (panel A), and a competing method that uses a vector of summary statistics to the same end (FILET; panel B). These classifiers were both trained and tested on the same data sets which were simulated under a joint demographic history inferred from a sample of *Drosophila simulans* and *D. sechellia* individuals (as described in the Methods) with and without introgression. The classifiers seek to discriminate among three classes: no introgression in the genomic window being examined, introgression from *D. sechellia* to *D. simulans*, and introgression from *D. simulans* into *D. sechellia*. Each entry in the matrix shows the fraction of test examples belonging to the class specified on the y-axis that were inferred by the method to belong to the class specified on the x-axis. Correct classifications are those found along the diagonals, while all off-diagonal entries represent incorrect classifications.

294

295 Researchers have thus sought to devise methods capable of detecting introgressed regions
296 from multispecies population genomic data sets. These include methods that attempt to infer the
297 ancestry for each individual at each site (e.g. Price *et al.* 2009; Lawson *et al.* 2012; Sohn *et al.* 2012)
298 and those that explicitly seek to discriminate between introgressed and non-introgressed loci

299 (Sankararaman *et al.* 2014; Geneva *et al.* 2015; Rosenzweig *et al.* 2016; Schrider *et al.* 2018). We
300 trained a CNN to identify introgression in a scenario modeled after the demographic history of
301 the *Drosophila simulans*-*D. sechellia* species pair (Methods), for which there is evidence for recent
302 gene flow (Garrigan *et al.* 2012).

303 Fig. 4A displays the results of these tests in the form of confusion matrices, which show
304 the fraction of test examples correctly predicted for each class (diagonal values) as well as the
305 fractions incorrectly assigned (off-diagonal values). To compare the performance of our CNN to
306 competing approaches, Fig. 4B displays the confusion matrix for FILET, a method previously
307 shown to outperform several methods, including two statistics for detecting introgression (Joly *et*
308 *al.* 2009; Geneva *et al.* 2015), and a tool that infers local ancestry tracks for each individual
309 (Lawson *et al.* 2012). Overall, this CNN classified 88.5% of test simulations correctly (95%
310 confidence interval: 87.7–89.2%). The most difficult scenario for the CNN was introgression
311 from *D. simulans* into *D. sechellia*, which it misclassified as “no introgression” 23% of the time. For
312 the other two classes the CNN accuracy was >95%. Importantly, for every class this CNN
313 achieved greater accuracy than FILET (overall accuracy of 82.5%; 95% confidence interval:
314 81.7%–83.4%), a machine learning approach that leverages a vector of 31 summary statistics
315 (Schrider *et al.* 2018). Thus, it is a useful measuring stick for assessing the CNN’s accuracy, and
316 the CNN’s success in this comparison is encouraging.

317

318 **Estimating historical recombination rates**

319 Recombination creates new combinations of alleles, and the degree of linkage between selected
320 sites affects the efficiency with which natural selection can act on each individual site (Hill and
321 Robertson 1966). The interplay of selection and recombination also influences the landscape of
322 diversity across the genome (Begun and Aquadro 1992). Knowledge of recombination rates is
323 thus key to population genetics research. As a more practical alternative to estimating rates
324 directly (e.g. from pedigrees; Kong *et al.* 2010), one can infer recombination rates from
325 population genetic data by examining associations among alleles at different sites. A number of
326 methods have been proposed to solve this problem, including summary statistic estimation
327 approaches (e.g. Hudson and Kaplan 1985; Hudson 1987; Hey and Wakeley 1997), composite
328 likelihood-based methods (e.g. Hudson 2001; McVean *et al.* 2004; Chan *et al.* 2012), and machine
329 learning tools using a vector of statistics (Lin *et al.* 2013; Gao *et al.* 2016). We sought to determine

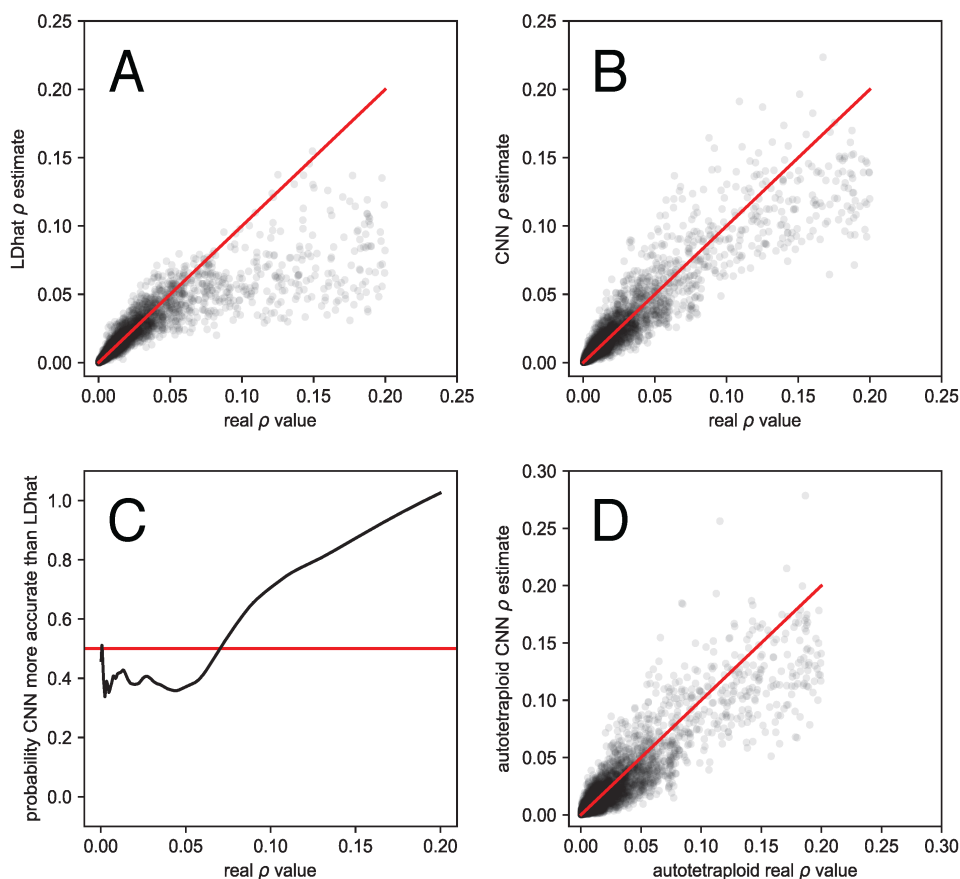


Fig. 5: Accuracy of recombination rate estimates from LDhat and our CNN. Panels A and B show the real ρ values per base pair on the x-axes and LDhat's (A) and the CNN's (B) predictions on the y-axes. Panel C again shows the real ρ values on the x-axis, and the probability that the CNN was more accurate than LDhat (black line) on the y-axis. This probability was calculated by scoring estimates where the CNN outperformed LDhat as one and the reciprocal as zero, and then smoothing these values with a lowess curve with a span of 15%. The red line represents the expectation if both methods had identical accuracy. Panel D shows the results from the simulated autotetraploid model, with the real ρ values on the x-axes and the CNN prediction on the y-axes.

330 whether a CNN taking an alignment image as input could be trained to tackle this task. To
331 address this problem, we first trained a CNN to estimate the historical population recombination
332 rate $\rho=4Nr$ (where r is the crossover rate per base pair per meiosis) from phased chromosomes.
333 This is the simplest scenario, as the arrangement of alleles on chromosomes is completely
334 resolved. Following training, we compared the CNN's performance to that of LDhat (McVean
335 *et al.* 2004), a widely used composite likelihood method, on the same testing data (Fig. 5). We
336 generated a test set of alignments whose values of ρ spanned three orders of magnitude, from
337

338 0.0002 to 0.2 (expressed per bp). Overall, both approaches performed well at predicting the true
339 value of ρ . **LDhat** had an $R^2 = 0.77$ and an RMSE = 0.016, whereas the CNN had a $R^2 = 0.86$
340 and an RMSE = 0.011 (Fig. 5A,B). **LDhat** appears to estimate ρ slightly better than the CNN
341 for lower recombination rates, whereas the CNN performs better at the higher values of ρ (Fig.
342 5C). Additionally, the CNN appears to provide a roughly unbiased estimator of ρ , while **LDhat**'s
343 estimates appear downwardly biased.

344 Because the CNN was capable of estimating ρ independent of θ , we were interested to see
345 how well it could interpolate between the θ values it was trained with. The CNN was trained with
346 a large gap between $N = 20,000$ and $N = 50,000$ (and thus a large gap in θ ; see Methods), so we
347 used coalescent simulations to generate an additional test set with N values drawn uniformly
348 among 30,000, 35,000, 40,000, and 45,000. When tested on these data the CNN's predictions
349 had an $R^2 = 0.82$ and an RMSE = 0.017. This represents a slight decrease in accuracy from the
350 values obtained when tested on the same N values used in training, but nonetheless shows that
351 the CNN can interpolate between training parameters without a dramatic loss in accuracy. This
352 could be a useful property, for example in cases where N (or θ) is unknown, but where one can
353 generate coalescent simulations across a range of plausible values.

354 Further complications arise when estimating ρ from unphased data. Under this scenario
355 the arrangement of alleles on chromosomes is not known. One work-around is to first phase the
356 alleles and then infer ρ as above, but not all data sources are easily phased, and phasing errors
357 will, of course, reduce accuracy. Another approach is to analyze the unphased data directly. The
358 relevant theory required to tackle this problem in a probabilistic manner has been worked out for
359 unphased diploids (Auton and McVean 2007), but expanding this theory to higher ploidies would
360 require a substantial effort. Take for example an autotetraploid with tetrasomic inheritance,
361 where there are five possible genotypes ($AAAA$, $AAAa$, $AAaa$, $Aaaa$, and $aaaa$). To further
362 complicate things, after sequencing an autotetraploid genome to a moderate depth of coverage
363 and identifying polymorphisms, the true underlying genotype may be uncertain. For example,
364 given a site with 10 reads supporting A and 10 supporting a , the true genotype could be $AAAa$,
365 $AAaa$, or $Aaaa$. To show the utility of CNNs in addressing novel population genomic inference
366 problems, we designed a CNN capable of inferring ρ from a simulated set of sequence reads from
367 an unphased autotetraploid population sample.

368 We used a simple simulation scheme to produce read counts for each allele at each site
369 for each individual in a sample of 12 autotetraploids, each with approximately 25X expected
370 genome-wide coverage (see Methods). Rather than allelic assignments, the input matrix for this
371 CNN contains for every site in each individual the fraction of reads bearing the a allele. Deriving
372 a likelihood function for ρ under this formulation may be challenging, and such a solution has not
373 yet been attempted. However, appropriately designed artificial neural networks are universal
374 approximators, meaning that they have the potential to approximate any continuous function
375 over a compact input space (Hornik 1991). Thus it is possible for a CNN to approximate the
376 desired likelihood function, even in its absence. To this end we trained a CNN with a similar
377 architecture to the one used above on phased haploid chromosomes (see Methods). We evaluated
378 the performance of this CNN on a set of simulations where ρ again ranged from 0.0002 to 0.2
379 (still scaling by $4N$, rather than $8N$ which would be appropriate for tetraploids, so the result can
380 be compared to those above). The CNN's predictions had an $R^2 = 0.83$ and an RMSE = 0.012
381 (Fig. 5D). As before, the estimate of ρ was made independent of θ , which varied over an order of
382 magnitude. The fact that this autotetraploid network performed only slightly worse than the
383 haploid version demonstrates that a CNN can solve problems for which no model-based
384 likelihood (or even composite likelihood) approach has been obtained, empowering empiricists
385 untrained in methods development to address questions specific to their biological system.

386

387 **CNNs can accurately detect and categorize signatures of recent positive selection**

388 When a new mutation is immediately favored by positive selection, it rapidly increases in
389 frequency until it fixes (i.e. completely replaces all other alleles at that site). This phenomenon,
390 referred to as a hard selective sweep, drastically reduces the amount of linked neutral variation
391 (Maynard Smith and Haigh 1974), and produces characteristic skews in the allele frequency
392 spectrum (Fay and Wu 2000) and linkage disequilibrium at linked sites (Kim and Nielsen 2004).
393 Alternatively, in a process known as a “soft sweep” populations may adapt via selection on a
394 polymorphism that has been segregating for some time, such that the adaptive allele exists on
395 numerous haplotypes (Hermisson and Pennings 2005). To uncover the mode of recent
396 adaptation and the genomic regions underlying recent adaptation, a large number of methods
397 have been devised to detect and characterize selective sweeps. These include summary statistics
398 (Kelly 1997; Fay and Wu 2000; Kim and Nielsen 2004; Voight *et al.* 2006; Garud *et al.* 2015),

399 composite likelihood-based approaches (Kim and Stephan 2002; Kim and Nielsen 2004; Nielsen
 400 *et al.* 2005; Vy and Kim 2015), and supervised machine learning approaches using a vector of
 401 statistics to obtain greater power than individual tests/statistics (Lin *et al.* 2011; Pybus *et al.* 2015;
 402 Schrider and Kern 2016; Sheehan and Song 2016; Sugden *et al.* 2018). Although these efforts
 403 have led to considerable progress, detecting and distinguishing between hard and soft sweeps
 404 remains a major challenge.

405 We built a CNN to detect selective sweeps and to discriminate between hard sweeps and
 406 soft sweeps. This CNN follows the S/HIC method of Schrider and Kern (2016) by casting the
 407 problem as a classification task where the genomic region being examined is assigned to one of
 408 five disjoint classes: a recent classic “hard” sweep, a recent “soft” sweep, a region linked to a
 409 nearby hard sweep, a region linked to a nearby soft sweep, or a neutrally evolving region.

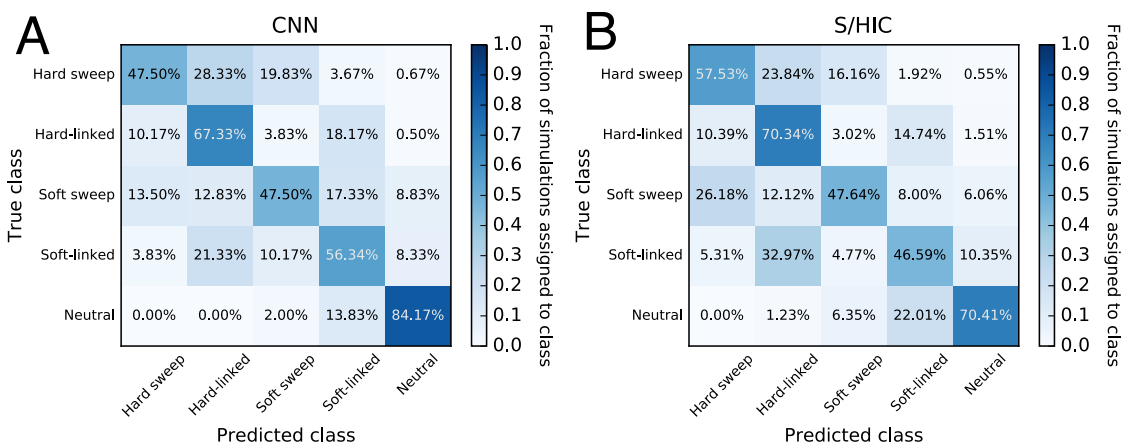


Fig. 6: Confusion matrices showing accuracies of two methods that seek to detect recent positive selection by discriminating among hard sweeps, soft sweeps, unselected regions closely linked to hard and soft sweeps, and neutrally evolving regions. (A) Confusion matrix summarizing the performance of our CNN, which uses an alignment image as input. (B) Performance of S/HIC, which uses a vector of summary statistics each measured in windows surrounding the region to be classified. These two classifiers were both trained and tested on the same data sets described in the Methods.

410 Like FILET for the problem of detecting introgression, comparing the CNN’s accuracy to
 411 that of S/HIC is informative because S/HIC was previously shown under a variety of simulated
 412 scenarios to have greater power than a number of competing methods (Schrider and Kern 2016).
 413 Rather than adopting S/HIC’s approach of using a large vector of statistics, the CNN takes an
 414 alignment image as input. We tested both methods against data simulated under a challenging
 415 demographic history estimated from human population data (Methods). As evidenced by the
 416

417 confusion matrices in Fig. 6, the CNN has slightly higher overall accuracy than S/HIC (60.6%
418 with 95% confidence interval: 58.8–62.3% for the CNN; versus 58.5% with 95% confidence
419 interval: 56.7%–60.2% for S/HIC). While S/HIC appears to be somewhat more sensitive to
420 sweeps, the CNN achieves a more than 3-fold reduction in false positive rate: 2% of neutral
421 simulations are classified as sweeps by the CNN, versus 6.35% for S/HIC; all of these false
422 positives are classified as soft sweeps. This quality may be particularly desirable when scanning
423 genomes where sweeps are relatively rare and thus a high degree of specificity is required to
424 maintain a low false discovery rate, although the proclivity of either classifier to produce false
425 positives versus false negatives can be adjusted by imposing a posterior probability cutoff. Note
426 that these classifiers were both trained under the same demographic history from which the test
427 data were generated. We would not expect this CNN to match S/HIC’s robustness to
428 demographic misspecification given that S/HIC’s feature vector was designed with this in mind,
429 though we did not test this. Nonetheless, the fact that the CNN has similar accuracy to S/HIC
430 under this difficult test scenario is highly encouraging.

431

432 **CNNs can extract demographic information from alignments**

433 A major focus of population genetics research is to use genomic data to elucidate species’
434 demographic histories—the extent and timing of population size changes, and the history of
435 population splits and migration events. For example, a host of population genetic approaches
436 have been devised to infer the times and intensities of population contractions and expansions
437 over the course of a species’ recent history (e.g. Marth *et al.* 2004; Schiffels and Durbin 2014; Liu
438 and Fu 2015), and to elucidate the history of population splits and subsequent gene flow (Nielsen
439 and Wakeley 2001; Hey 2009), and population merging events (e.g. Lipson *et al.* 2013; Loh *et al.*
440 2013). We asked whether CNNs can effectively extract demographic information from alignment
441 images, focusing on the task of inferring population size histories. In particular, we attempted to
442 train a CNN to estimate the parameters of a three-epoch model of instantaneous effective
443 population size changes. There are five such parameters: the ancestral population size (N_2), the
444 time of the more ancient population size change (T_2), the population size after this change (N_1),
445 the time of the more recent change (T_1), and the present-day population size (N_0); our response
446 variable is the vector of these 5 real-valued parameters. Thus this analysis also allows us to assess
447 the ability of CNNs to predict multiple population parameters simultaneously.

448

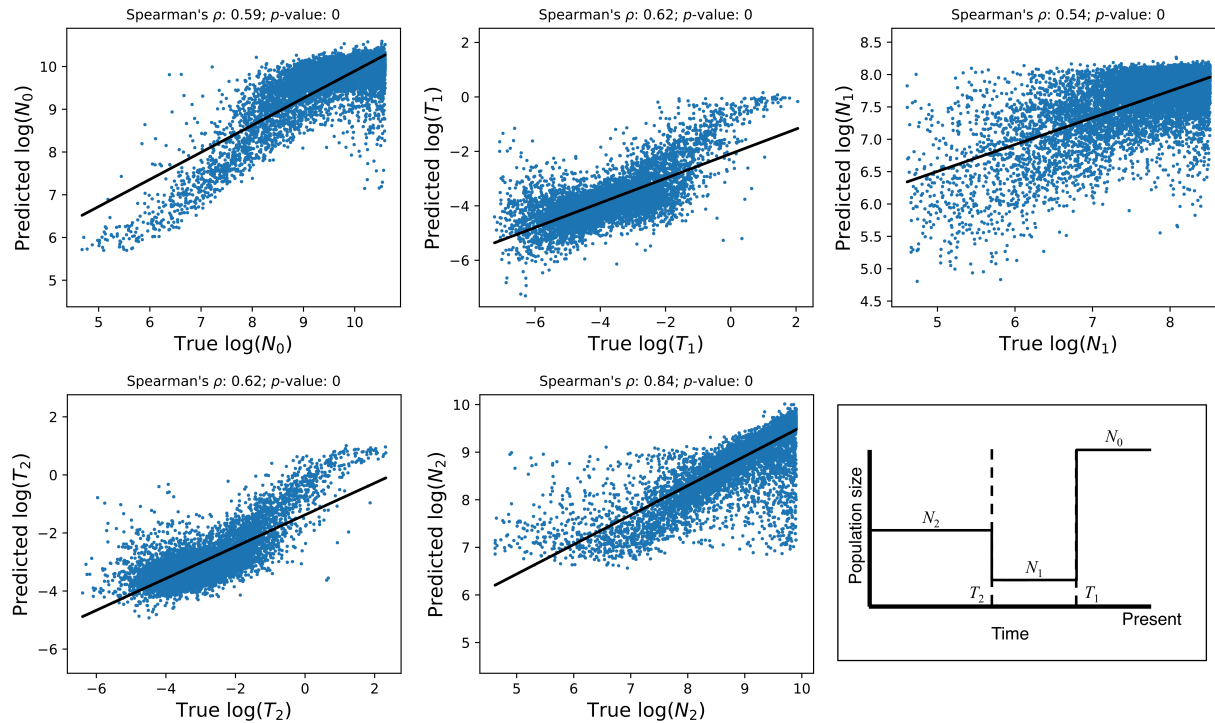


Fig. 7: Accuracy of demographic inference CNN. The scatterplots show the correlation between true and predicted demographic parameter values using our best-performing CNN for this task when applied to an independent test set. Note that there may be some monotonicity in the relationship between the true and predicted values of some of these parameters, which may affect calculations of the Spearman correlation coefficients shown above each scatterplot. These estimates should thus be viewed as a rough summary of this relationship, while the RMSE values reported in the text better summarize our accuracy. The inset on the bottom right shows the demographic model and its five parameters.

449

450

451

452

453

454

455

456

457

458

459

We simulated 50 haploid chromosomes under a variety of randomly selected population size histories, and trained a CNN to estimate the demographic model parameters. The simulated region was roughly equivalent in length to 1.5 Mbp of the human genome (Methods). Because we found this problem to be comparatively difficult, we experimented with a variety of hyperparameters governing the neural network structure and input/output format. In supplementary table S1 we show the optimal RMSE (i.e. the minimum RMSE across training iterations) for each hyperparameter combination examined. This experiment revealed several general trends. First, 1D convolutional networks tended to fare slightly better than their 2D counterparts (median RMSE of 0.52 across all hyperparameter combinations with 1D convolutional filters, and median RMSE 0.54 for 2D convolutions; $p=1.1 \times 10^{-4}$; Mann-Whitney

460 U test); however several 2D networks performed nearly as well as the best 1D network, achieving
461 an RMSE of <0.5 while the best score obtained overall was 0.43. Second, smaller convolutional
462 filters tended to perform slightly better than larger ones—we observed a positive correlation of
463 kernel size with RMSE across hyperparameter combinations ($\rho=0.26$; $p=6.9\times 10^{-4}$; Mann-
464 Whitney U test). For example, the median validation RMSE was 0.51 for a kernel size of 2 versus
465 0.56 for a kernel size of 10. Third, log-scaling the demographic parameters to be estimated
466 increased accuracy (RMSE decreased from 0.55 to 0.52; $p=0.020$; Mann-Whitney U test). For
467 this problem sorting chromosomes by relatedness resulted in a small improvement (RMSE
468 decreased from 0.54 to 0.53; $p=0.034$). Encoding ancestral and derived alleles as ‘0’ and ‘255’
469 (i.e. black and white in a grayscale image), respectively, versus ‘-1’ and ‘1’ had a significant
470 influence on accuracy, with the former yielding better performance than the latter (RMSE of
471 0.51 vs. 0.60; $p=1.5\times 10^{-15}$). Finally, using dropout resulted in a slight decrease in accuracy
472 (median RMSE increased from 0.52 to 0.55) though this was not statistically significant
473 ($p=0.092$). We note that these trends may change if the amount of training data is increased or
474 decreased, and may not necessarily hold for other tasks.

475 In Fig. 7, we show the correlation between the true and inferred values for each of these 5
476 parameters for the best performing network. For N_0 and T_0 , these correlations are quite high,
477 implying that our CNN can recover the true values reasonably well. However, for the remaining
478 parameters, the correlation is lower (though still highly significant), and our CNN produces
479 downwardly biased estimates when the values of these parameters are larger. Although our
480 accuracy is far from perfect, we consider these results fairly encouraging because we are only
481 examining a single moderately sized genomic region, while other modern demographic inference
482 methods use data from across the genome. For example, $\partial a \partial i$ (Gutenkunst *et al.* 2009) uses allele
483 frequencies measured at a large number of polymorphisms (e.g. those found in all distal
484 intergenic regions across the genome; Gazave *et al.* 2014). PSMC and MSMC (Li and Durbin
485 2011; Schiffels and Durbin 2014) take data from a single very large recombining region such as
486 an entire chromosome. In essence, we are currently only able to utilize information about the
487 coalescent histories of the region in question—and this collection of histories may not match that
488 of the entire population, which would be more accurately reflected in genome-wide data. In the
489 Discussion, we address prospects for incorporating genome-scale data in demographic inference.
490

491 **DISCUSSION**

492 **Convolutional neural networks are well suited for population genetic problems**

493 Population geneticists have devised a wide array of computational methods to make evolutionary
494 inferences from genomic data. Typically the goal of these efforts is to aggregate information
495 across genomic sites in order to make an accurate inference. These methods include likelihood-
496 based approaches (e.g. Kim and Stephan 2002; Nielsen *et al.* 2005; Gutenkunst *et al.* 2009; Liu
497 and Fu 2015), probabilistic graphical models such as hidden Markov models (e.g. Turner *et al.*
498 2005; Boitard *et al.* 2009; Lawson *et al.* 2012), and those that rely on the use one or more
499 summary statistics designed to characterize patterns of variation within a genomic region (e.g.
500 Tajima 1989; Fu and Li 1993; Kelly 1997; Fay and Wu 2000; Kim and Nielsen 2004; Voight *et*
501 *al.* 2006; Ferrer-Admetlla *et al.* 2014). While these approaches differ substantially from one
502 another, they all have one thing in common: they make use of population genomic theory to
503 connect the features of a data set to the underlying evolutionary process. Here we have
504 demonstrated the potential of an alternative approach: treating population genetic inference as
505 an image recognition problem where the “image” is the population genetic alignment, which is
506 directly fed as input to a CNN. In contrast to most mainstream approaches, this CNN approach
507 makes use of the entirety of the data, rather than using theoretically derived estimators or closed-
508 form likelihood functions to connect a small number of features of the data to an evolutionary
509 process.

510 Here we have shown that CNNs perform remarkably well on a number of problems in
511 population genetics. We developed CNNs with comparable if not greater power to detect
512 selective sweeps, identify introgressed loci, and infer local recombination rates when compared to
513 current methods on simulated data sets. The CNNs for detecting sweeps and introgression
514 demonstrate the ability to use an alignment image to distinguish among multiple evolutionary
515 models, while the recombination rate estimator demonstrates that continuous parameters can
516 also be inferred. Finally, although our demographic parameter estimates were fairly imprecise,
517 they were only based on a short stretch of the genome, and nonetheless demonstrate that CNNs
518 have the potential to infer multiple parameters from a sequence alignment. While we were in the
519 process of preparing this manuscript, Chan *et al.* completed an important study demonstrating
520 that a CNN can accurately detect recombination hotspots (Chan *et al.* 2018). Taken together

521 these results suggest that CNNs have enormous potential as a general paradigm for population
522 genetic inference.

523 The effectiveness and generality of CNNs in population genetic inference should not be
524 surprising. CNNs offer a number of intrinsic advantages that make them particularly amenable
525 to population genetic data. First, there have been a number of efforts to move in the direction of
526 making inferences on the basis of the full complement of data present in an alignment rather
527 than one or more summary statistics (Li and Stephens 2003; Lawson *et al.* 2012; Smith *et al.*
528 2018). CNNs represent a natural way of examining the entirety of an alignment in order to
529 increase inferential power. The development of novel CNN architectures to better handle spatial
530 associations in the data across multiple scales (Yu and Koltun 2015) has the potential to improve
531 CNN-driven population genetic inference even further. For example, improved ability to detect
532 both the localized reduction in diversity at a sweep (Maynard Smith and Haigh 1974) as well as
533 the potentially confounding skews in patterns of diversity produced in its flanking regions
534 (Schrider *et al.* 2015) would be beneficial in sweep detection.

535 Another desirable property of CNNs is that they effectively perform automated feature
536 detection (LeCun *et al.* 2015). Because they discover discriminatory information directly from the
537 image, there is no need to manually construct an optimal set of features. CNNs may thus
538 outperform methods based on a set of manually curated features as observed here, although this
539 may not be the case for all tasks (e.g. Bellot *et al.* 2018). This brings up perhaps the strongest
540 quality of CNNs in the context of evolutionary inference: because CNNs can make inference in
541 the absence of statistics or a likelihood function, they can make predictions for phenomena for
542 which there exists no analytical expectation.

543 Indeed, CNNs can tackle problems for which no relevant summary statistics have been
544 devised—vectors of such statistics are required for other likelihood-free methods such as ABC
545 (Beaumont 2010) or traditional supervised machine learning techniques (Schrider and Kern
546 2018). On a related note, neural networks are particularly amenable to the incorporation of
547 disparate data types with no prior knowledge of their relationships. For example, here we have
548 included both genotype information and positional information for segregating sites as branches
549 to our networks, allowing both to be used together in prediction despite the fact that our network
550 isn't instructed how these two pieces of information relate to one another. All that is required is
551 appropriate training data. Thus, we may not have to wait for theoretical advances in order to

552 draw inferences from data, provided we are concerned with evolutionary models for which
553 training data can be obtained from simulation—including the wide range of scenarios that could
554 potentially be investigated via increasingly flexible and efficient forward simulators (Thornton
555 2014; Haller and Messer 2017; Kelleher *et al.* 2018).

556 This point is driven home by the success of our CNN for estimating recombination rates
557 in autotetraploids from read pileup information alone—despite the input’s lack of genotype calls,
558 let alone phased haplotypes, these inferences are nearly as accurate as those that we obtained
559 from haplotype alignments. This result also suggests that CNNs may be well suited for other
560 inferences where genotype calls are unreliable (e.g. low coverage sequencing data; Korneliussen *et*
561 *al.* 2014) or unobtainable (e.g. pooled population sequencing; Schlötterer *et al.* 2014). Given
562 CNNs’ flexibility, future studies should evaluate their potential to tackle not only those problems
563 examined in this paper, but the myriad additional important challenges in evolutionary genetics
564 to which they could be readily applied, including but not limited to uncovering adaptive
565 introgression (Racimo *et al.* 2016), joint inference of selective and demographic histories (Sheehan
566 and Song 2016), and even inferring structured outputs such as ancestral recombination graphs
567 (Rasmussen *et al.* 2014).

568

569 **To what extent are CNNs robust to model misspecification?**

570 Another particularly encouraging result of our recombination rate estimation analysis is that we
571 were able to infer rates for data generated from a range of parameter values to which the CNN
572 had not been exposed during training with very little decrease in accuracy. This ability to
573 interpolate between training values is a particularly desirable property. First, it implies that
574 CNNs can be used to create flexible inference tools using a modest training data set, and second
575 that researchers can focus training between reasonable parameter bounds, without knowing the
576 true (and often unknowable) underlying parameters; future efforts must explore the possibility of
577 training networks to be robust to more extreme cases of model misspecification.

578 One illustrative example of the potential pitfalls of model misspecification is the problem
579 of detecting selective sweeps without accounting for confounding demographic events. For
580 example, population bottlenecks will skew genealogies in a manner similar to sweeps (Simonsen *et*
581 *al.* 1995), and thus may result in a large fraction of false positives (Jensen *et al.* 2005; Nielsen *et al.*
582 2005). Schrider and Kern (2016) were able to mitigate this problem by designing a feature vector

583 that is sensitive to the spatial skews in patterns of variation created by a sweep but insensitive to
584 genome-wide skews produced by demographic events. Although this strategy is not possible with
585 CNNs because they perform automated feature extraction, it may be that incorporating training
586 examples generated under potentially confounding scenarios could alleviate this issue.

587 Therefore, future work must thoroughly 1) assess how CNNs trained on data simulated
588 under one range of evolutionary parameters fare when applied to different parameterizations,
589 and 2) determine whether robustness to such misspecification might be achieved by training a
590 CNN under a wide range of parameter values that are likely to encapsulate the correct values—
591 the recombination rate estimator’s successful interpolation suggests that this may be a possibility.
592 Model misspecification is not a concern for tasks where training data may be obtained without
593 simulation (e.g. detecting selective constraint; Schrider and Kern 2015), though in such cases one
594 must take care to prevent dependencies between training and test examples because of shared
595 evolutionary histories due to physical linkage or paralogy/orthology relationships (Washburn *et*
596 *al.* 2018).

597
598 **Outstanding practical challenges associated with the application of CNNs to**
599 **sequence data**

600 Although the CNN approach outlined above has great potential, there are several outstanding
601 challenges with applying CNNs to a wider spectrum of problems. One important obstacle is the
602 large amount of training data required by CNNs, which makes applications requiring alignments
603 of large regions (e.g. entire chromosomes) more difficult. This challenge includes both the
604 generation of large labeled training examples, and time- and memory-efficient training with these
605 large examples given limited computational resources. Fortunately, continued improvements in
606 simulation speed (Kelleher *et al.* 2016; Kelleher *et al.* 2018) and the efficiency of CNN training
607 (Chilimbi *et al.* 2014; Yu and Koltun 2015; Jouppi *et al.* 2017; Köster *et al.* 2017) is mitigating this
608 problem. Such advances would be a boon for efforts to infer demographic parameters, which
609 require simultaneously examining data sampled from across the genome or along an entire
610 chromosome, unlike scans to infer locus-by-locus histories of
611 selection/recombination/introgression. Advances in handling large or high-resolution images
612 may also prove fruitful. For example, CNN-based strategies that simultaneously examine a
613 number of smaller “patches”, each covering a portion of the image rather than the entirety of the

614 image (e.g. Lu *et al.* 2015), may aid efforts to extract demographic information from genome-
615 scale data.

616 Another challenge with the application of CNNs is that their performance can be
617 sensitive to network architecture (Szegedy *et al.* 2015). There is no underlying theory for selecting
618 optimal network architecture, though improved architectures are sure to continue to arise, and
619 automated methods exist for optimizing the many hyperparameters of a given architecture (e.g.
620 Snoek *et al.* 2012). Though we uncover some promising CNN architectures for population
621 genetic inference, we suspect that substantial improvements can still be made.

622 We have also demonstrated that CNNs are sensitive to the input format of the population
623 genetic alignment, and our work has yielded several insights along this front. First, we found that
624 the ordering of haplotypes within the alignment can impact accuracy, and our results suggest that
625 it is often beneficial to reorder haplotypes so that more similar chromosomes appear next to one
626 another. This may be a suboptimal solution, and more creative approaches may be required to
627 provide a more general strategy. To this end, research into permutation-invariant neural
628 networks (Zaheer *et al.* 2017) may prove promising when dealing with sequence alignments. This
629 is evidenced by Chan *et al.*'s recent findings that a permutation-invariant architecture improves
630 both training speed and final accuracy of their CNN for detecting recombination rate hotspots
631 (Chan *et al.* 2018). Chan *et al.*'s network avoids any convolution or pooling operations that
632 combine information across individuals until an operation that collapses each column of the
633 (filtered) alignment matrix down to a single value in an order-invariant manner (e.g. site-wise
634 maximum). This design choice means that permuting the order of individuals within the
635 alignment will have no impact on their network's output. We also observed that 1D convolutions
636 in the proper orientation perform as well as the more widely used 2D convolutions in many
637 cases. Also, scaling response variables for regression problems (both log-scaling and
638 standardization) may also affect accuracy. We therefore recommend that users experiment with
639 these different ways of representing their data, as well as different CNN architectures, in order to
640 find the design that works best for the task at hand.

641 Another important consideration of CNNs is that once trained, they are specialized to a
642 particular problem as defined by the training set. That is, a CNN trained to infer recombination
643 rates under a European demographic history may have reduced accuracy when applied to an
644 African sample. Training under a variety of demographic scenarios may make a CNN more

645 robust to this problem, but a question for further study is whether this can be accomplished
646 without a loss in power relative to a more specialized CNN. Even a change as subtle as adding
647 another chromosome to a dataset will make one of our previously trained CNNs inapplicable, as
648 the input matrix would no longer be the proper size and either a new CNN must be trained or
649 the data subsampled. Importantly, Chan et al. (2018) describe an architecture that can allow for
650 variation in the number individuals in the input matrix. In spite of these limitations, recent
651 advances have greatly simplified training CNNs, and it will often be practical—or even
652 preferable—for a researcher to create a CNN tailored to their specific data set.

653

654 **Are CNNs a black box?**

655 Artificial neural networks are algorithms that seek to maximize their predictive accuracy by
656 optimizing their internal mathematical operations on training data and CNNs are an extremely
657 flexible subclass of these methods because they can act directly on the input data matrix (in our
658 case a sequence alignment). However, one consequence of this is that CNNs are in some ways a
659 “black box”. For example, a CNN cannot “explain” why it made a particular prediction given its
660 input. Supervised machine learning algorithms in general have perhaps been unfairly maligned
661 with this “black box” label. These methods can in principle reveal much about underlying
662 processes by determining which features are most informative under certain scenarios (i.e. feature
663 ranking; see Breiman 2001). For example, the observation that certain features are highly
664 informative for recent but not ancient introgression (Schridder *et al.* 2018) suggests some key
665 differences between the genealogies produced under these two scenarios. Due to their complex
666 inner workings, less progress has been made in breaking through the CNN “black box” as
667 compared to more traditional supervised machine learning techniques. However, some successful
668 explanatory tools are available for CNNs (Ribeiro *et al.* 2016), and there is ongoing research in
669 this area. Moreover, because the CNN framework we adopt here works on images, it may be
670 possible to translate future breakthroughs in CNN interpretation from other fields (e.g. image
671 recognition) into population genetic inference. Thus a more optimistic view is that as CNNs and
672 related methods become more interpretable, these likelihood-free image recognition approaches
673 may help to reveal theoretical insights into evolutionary processes.

674 In the near-term, CNNs may remain useful only as a predictive tool, and we will continue
675 to rely on theoretical advances to improve our understanding of population genetic processes. In

676 spite of the shortcomings noted above, the highly encouraging results that we have laid out here
677 suggest that CNNs are able to discover information about the underlying genealogies from
678 alignment images and to use this information to more accurately elucidate the evolutionary
679 phenomena that have shaped these genealogies. CNNs have enormous potential for population
680 genomic inference. We believe that progress on a host of problems could accelerate appreciably
681 were this technology to be embraced by the field. Indeed, when it comes to the business-end of
682 population genetics—drawing accurate evolutionary inferences from data—we predict that
683 increasingly, likelihood-free approaches such as the ones we have describe here will prove most
684 effective at solving existing problems, and expand the universe of problems that researchers can
685 investigate.

686

687 **MATERIALS AND METHODS**

688

689 **Computational environment for training CNNs**

690 All CNNs used in this study were developed using two open source Python packages: Keras
691 (version 2.0.6; <https://keras.io/>) to define neural network architecture and orchestrate training
692 and testing, and TensorFlow (version 1.1.0; <https://www.tensorflow.org/>) as the backend (i.e.
693 TensorFlow performs the computation during training/testing). CNN training is computationally
694 intensive, but cloud-based GPU resources have made it affordable. As an example, our network
695 for detecting selective sweeps was trained on a cloud-based system with one Nvidia K80 GPU. It
696 took 6.6 hrs to train, and at \$0.90 US dollars per hour the total cost was under \$7. All code used
697 for training is available online (https://github.com/flag0010/pop_gen_cnn).

698

699 **CNN validation strategy**

700 For each task, we divided our simulated inputs into three sets: a training set, a validation set, and
701 a test set. The training set was used to optimize the weights and biases of the CNN. The
702 validation set was used during training to determine how well the CNN generalizes to unseen
703 data, and adjustments were made to the CNN to improve its performance on the validation data.
704 We also used the validation set to terminate training once accuracy on this set appeared to
705 plateau—this process took different numbers of iterations for different tasks. Finally, the test set
706 was used to obtain a performance assessment of the final trained network. Importantly, this test

707 set was previously unseen by the CNN and therefore yields an unbiased evaluation of its
708 accuracy. We used `binom.test` in R to estimate 95% confidence intervals for classification
709 accuracies.

710

711 **Evaluating techniques for rescaling and reordering inputs to improve CNN** 712 **accuracy**

713 To evaluate the impact of alternative data preparation techniques, we developed a simple CNN
714 that estimates the locus-wide population mutation rate $\theta=4N\mu L$ where μ is the mutation rate per
715 base pair per generation and L is the physical length of the locus being examined. This CNN is
716 trained using alignment images with forty chromosomes and θ drawn uniformly between 10 and
717 50 as simulated for a panmictic, constant sized population by `ms` (Hudson 2002). We trained this
718 CNN to minimize the root mean squared error (RMSE) between its prediction and the true value
719 of θ using 4,000 training matrices. Then its accuracy was scored on 1,000 test matrices that the
720 CNN was never trained on. These values were compared under different data preparation
721 approaches described below.

722 First, the matrices output by most coalescent simulation software, including `ms`, encode
723 ancestral and derived alleles for biallelic sites as 0 and 1, respectively, and present the matrix
724 with phased haploid chromosomes as rows and sites as columns. When doing 1D convolutions,
725 we sought to use row-wise convolutional filters (Fig. 1C), i.e. those that examine each
726 chromosome in our sample across a small number of contiguous segregating sites (specified by
727 the “kernel_size” parameter in Keras) before sliding the filter forward one site (our stride length,
728 “strides” in Keras, was always set to 1). At present Keras does not allow for row-wise 1D
729 convolutions, so we accomplished this by transposing the alignment matrix and performing
730 column-wise convolutions.

731 We also assessed the impact on accuracy of sorting the chromosomes in the alignment by
732 genetic similarity. For example, the matrices in Fig. 2 contain identical information, but
733 chromosomes in the matrix on the left are randomized, while on the right they are sorted by
734 genetic similarity. We offer a fast algorithm for sorting matrices by genetic similarity
735 (https://github.com/flag0010/pop_gen_cnn/blob/master/sort.min.diff.py).

736

737 **Introgression detection**

738 To detect introgression, we simulated phased haploid training and test examples with **msmove**
739 (<https://github.com/geneva/msmove>) from the same demographic model that Schrider et al.
740 (2018) used to train the FILET classifier for detecting introgression between *Drosophila simulans*
741 and *D. sechellia*. In total we produced 237,500 coalescent simulations from 3 classes: 112,500
742 without no migration between species (No Introgression), 112,500 with gene flow from *D.*
743 *simulans* into *D. sechellia* (*sim*→*sech*), and 12,500 with gene flow from *D. sechellia* into *D. simulans*
744 (*sech*→*sim*). We used fewer *sech*→*sim* examples because test runs on smaller training sets suggested
745 that the network could detect this class fairly accurately, which allowed us to increase the
746 sampling of the other two more challenging classes by simulating more examples from them. To
747 our knowledge this approach of intentionally inflating the number and proportion of training
748 examples from the more challenging classes is unusual, as typically a balanced training set is
749 preferred. However we found that including additional examples from classes into our data set
750 substantially improved our ability to correctly them. The simulations were randomly assigned to
751 training and validation sets so that the training set included 107,500 examples each from the No
752 Introgression and *sim*→*sech* classes, and 7,500 examples from the *sech*→*sim* class. Both the
753 validation set and the test set contained 2,500 of each class (i.e. 7,500 total). Importantly, because
754 our test and validation sets were evenly balanced, they provided unbiased estimates of our
755 accuracy.

756 As in the *Drosophila* data set to which Schrider et al. applied FILET, each of our
757 coalescent simulations generated 34 chromosomes (14 *D. sechellia* and 20 *D. simulans*). Each
758 column in the alignment corresponded to a biallelic polymorphism, which was encoded as “0”
759 (ancestral allele) or “1” (derived allele) for each chromosome. In practice, the ancestral and
760 derived states may not be known with 100% certainty, and one may instead use major/minor
761 alleles, or randomly mispolarize a fraction of sites in the training data if one has an estimate of
762 the fraction of mispolarized sites in the true data. The effects of these design choices on
763 performance may then be evaluated on test data. Each matrix was organized so that individual
764 chromosomes were grouped by species. Each coalescent simulation produced a different number
765 of segregating sites (with the largest containing 1201 polymorphisms). Because the CNN’s input
766 matrices must all have the same dimensions, we padded the right side of all matrices with fewer
767 than 1201 polymorphisms with columns containing only “0” until the total number of columns
768 reached 1201. Finally we transposed this matrix resulting in a 1201×34 matrix for each

769 coalescent simulation. In practice, one will have to set the image width to the largest number of
770 SNPs encountered across all training, test/validation, or real data examples included in the
771 analysis. Alternatively, one may select a fixed number of segregating sites to include in the
772 analysis, in which case each example may correspond to a different physical size (creating
773 additional variance in total recombination rates). Thus, when using this alternative approach,
774 one should adjust the lengths of simulated examples accordingly.

775 We trained a CNN architecture with three 1D-convolutional layers (kernel size = 2), each
776 followed by average-pooling, and finally two densely connected layers (i.e. the same network
777 architecture as the main network branch illustrated in Fig. 1C, but with one additional dense
778 layer). These layers contained 256, 128, 128, 128, and 128 neurons, respectively. To avoid
779 overfitting during training, each layer used dropout regularization (randomly removing 25% of
780 neurons between convolutional layers during each training iteration, and 50% between densely
781 connected layers) and rectified linear unit activation functions (i.e. ReLUs; Hahnloser *et al.* 2000;
782 Nair and Hinton 2010). Dropout regularization encourages the CNN to learn redundant
783 representations of the data, thereby reducing the network's dependence on individual weights
784 (Srivastava *et al.* 2014). The last layer was a sigmoid output layer with 3 neurons, each
785 corresponding to the 3 classes given above. The CNN was trained using the Adam optimization
786 procedure (Kingma and Ba 2014), a categorical cross-entropy loss function, and a mini-batch size
787 of 256. The CNN was run for 19 training iterations through the training data.

788

789 **Recombination rate: phased haplotype version**

790 For the recombination rate estimator we used **ms** (Hudson 2002) to simulate 50 phased
791 chromosomes, each with a target length of 20kb. To do so, we drew a population size (N) from
792 the following values: 5,000, 10,000, 15,000, 20,000, and 50,000, and set the population-scaled
793 mutation rate parameter $\theta = 4N\mu L$ (letting $\mu=1.5\times 10^{-8}$ and $L=20\text{kb}$). We also set a population-
794 scaled recombination rate, $\rho = 4NrL$, where r is the per bp crossover rate per meiosis, by drawing
795 r from a bounded exponential distribution ranging from 10^{-8} to 10^{-6} . This yields a range of ρ per
796 base pair of 2×10^{-4} to 2×10^{-1} . These values roughly encompass the range of recombination rates
797 experienced in humans and *Drosophila*. Following this procedure, we generated 156,275
798 coalescent simulations. $\sim 92\%$ were used to train the CNN, and $\sim 4\%$ each were set aside for
799 validation and testing. To assess our CNNs ability to interpolate to unseen population sizes, we

800 also created 5,000 additional test matrices using the procedures above, but with N drawn
801 uniformly from the following: 30,000, 35,000, 40,000, and 45,000.

802 Each simulation was represented by a matrix of 50 rows, one for each chromosome, and
803 418 columns (the largest number of segregating sites). As before, we encoded the ancestral allele
804 with “0” and the derived allele with “1”. Because not all simulations resulted in the same number
805 of polymorphisms, we padded both the genotype matrix and the position vector in the same
806 manner as for the introgression CNN, bringing the total size of each matrix to 50×418 . Next, we
807 sorted each matrix by genetic similarity among chromosomes as described above and then
808 transposed the matrix to 418×50 . We also extracted the segregating site positions vector from the
809 `ms` output which represents each position as a real number between zero (the leftmost position
810 on the simulated chromosome) and one (the rightmost position). For simulations with fewer than
811 418 segregating sites, we padded the positions vector with “-1”s.

812 We transformed the ρ values for the training, validation, and test sets by taking the natural
813 log of each value and centering them on the mean of the training set. By using the mean from the
814 training set for all transformations, we ensure that there is no leakage of information between
815 training and validation/testing.

816 We trained a CNN with two input branches. The first branch took the haplotype
817 matrices as input and included three 1D-convolutional layers (kernel size = 2), each followed by
818 average-pooling. These layers contained 1250, 256, and 256 neurons, respectively. Each of these
819 layers uses dropout normalization (25%), L2-regularization of the weights ($\lambda = 0.0001$), and
820 ReLU activation functions. The second branch took the position vector as input and contains
821 one densely connected layer with 64 neurons, again using dropout normalization (10%) and a
822 ReLU activation function. The two branches are then merged into another densely connected
823 layer of 256 neurons with ReLU activation functions. Finally, the output layer is a single neuron
824 with a simple linear activation function that predicts the continuous ρ value. The CNN was
825 trained using the Adam optimization algorithm, using mean-squared error as our loss function,
826 and a mini-batch size of 32. The CNN was trained for 16 iterations.

827 We compared our CNN’s results to those of `LDhat` version 2.2a
828 (<https://github.com/auton1/LDhat>). We chose `LDhat` because it is widely used to estimate
829 historical recombination rates, and because it can be efficiently run on large data sets. `LDhat` will
830 estimate ρ only for a specified population mutation rate ($\theta = 4N\mu$), and we supplied it with the

831 exact θ value used for each coalescent simulation. This was done by creating five likelihood
832 lookup tables using the **complete** program, all set for 50 haploid chromosomes, for the
833 following θ values: 6, 12, 18, 24, and 60. Respectively, these correspond to $N = 5,000, 10,000,$
834 $15,000, 20,000,$ and $50,000$ (the same values we used for training our CNNs). **LDhat** only
835 predicts values within the bounds of the lookup table. Therefore, to facilitate a fair comparison to
836 results from our CNN, which is unbounded, we selected the maximum ρ value in the likelihood
837 lookup table to be 133.3% of the true maximum for each θ . We then set the grid size of ρ equal 1,
838 and estimated ρ on the test set using **LDhat**'s **pairwise** program.

839 In contrast, the CNN was not provided information about θ , and instead had to infer ρ
840 independent of θ . This ability would be a desirable property for an estimator, as θ is likely to vary
841 considerably across the genome and outside of simulated data sets one may never know θ
842 precisely. On the other hand, the CNN was provided with the physical distance between
843 segregating sites, information **LDhat** does not utilize but which will generally be available when
844 making inferences on real data. Both of these factors make our direct comparison of the CNN
845 with **LDhat** imperfect because each had access to information the other lacked when producing
846 its estimate. Nonetheless we consider this example a useful illustration of the CNN's
847 performance.

848

849 **Recombination rate: autotetraploid version**

850 We sought to train a CNN to estimate a locus-wide recombination rate in autotetraploid
851 genomes. To add a level of methodological realism to this problem, we did so from a matrix
852 storing a simple summary of read pileup information at each site for each individual.

853 To this end, we generated new coalescent simulations with 48 chromosomes each
854 following the procedure outlined above for the haploid CNN. This approach is reasonable
855 because it has been shown that the standard coalescent approximates the appropriate coalescent
856 for autotetraploids as long as N is larger than a few hundred (Arnold *et al.* 2012). We generated
857 217,500 coalescent simulations, and randomly assigned 200,000 to the training set, 10,000 to the
858 validation set, and 7,500 to the test set. Next, within each coalescent simulation, we randomly
859 partitioned our 48 chromosomes into twelve sets of four. Each set represents one synthetic
860 autotetraploid genome and every site has five possible genotypes (*AAAA, AAAa, AAaa, Aaaa,* and
861 *aaaa*). For each autotetraploid genome i and each site j we simulated the number of reads

862 covering the site (C_{ij}) by drawing a random sample from a Poisson distribution with $\lambda = 25$. Then
863 we selected the number of reads representing the a allele $R_{ij} \sim \text{Binom}(n=C_{ij}, p=x_{ij})$, where x_{ij}
864 represents the frequency of the a allele in the tetraploid genotype (i.e. 0, 0.25, 0.5, 0.75, and 1 for
865 the five genotypes listed above). For each individual i at site j , the corresponding entry in the
866 input matrix was the fraction R_{ij}/C_{ij} , i.e. the fraction of reads supporting the derived allele. The
867 $AAAA$ and $aaaa$ genotypes were always 0 and 1, respectively. For the three heterozygous
868 genotypes ($AAAa$, $AAaa$, and $Aaaa$), R_{ij}/C_{ij} varied based on sampling error but had expected values
869 of 0.25, 0.5, and 0.75, respectively. Thus at each site the original 48 chromosomes were reduced
870 to a set of 12 values corresponding to the fractions of reads supporting the a allele in a pool of
871 sequence reads from an autotetraploid sequenced at $\sim 25X$ coverage. Note that this scheme
872 includes neither sequencing error, nor the site-specific depth which would be necessary to
873 calculate a likelihood, but is nonetheless adequate for our proof of concept.

874 As above, we sorted the rows of this matrix by genetic similarity and padded each matrix
875 with zeros to a length of 460 (the most segregating sites of any of the simulated matrices) before
876 transposing, yielding a 460×12 matrix. Again, we recorded the padded vector of positions from
877 the simulation output. Our CNN architecture was identical to the one given above for the phased
878 haplotype version, except for the dimensionality of the input changed to 460×12 , and we
879 reduced the first convolutional layer from 1250 to 256 because of the smaller second dimension
880 of the input. The CNN was trained for 9 iterations.

881

882 **Detecting selective sweeps and discriminating between modes of selection**

883 For detecting selective sweeps, we used the same coalescent simulations that Schrider and Kern
884 (2017) used to train a classifier to detect sweeps in the JPT population (Japanese individuals from
885 Tokyo) from Phase 3 of the 1000 Genomes dataset (Auton *et al.* 2015). The JPT demographic
886 scenario is one where detecting selective sweeps is fairly difficult (see Figure S1 from Schrider and
887 Kern 2017), as expected for bottlenecked populations (Jensen *et al.* 2005). For this CNN, we
888 began with a set of 269,000 simulated genomic windows with the 5 following classes: a recent
889 hard sweep (i.e. fixation of a *de novo* beneficial mutation), a recent soft sweep (i.e. fixation of a
890 beneficial but previously neutral segregating polymorphism), a region linked to a nearby hard
891 sweep, a region linked to a nearby soft sweep, and a neutrally evolving region. Each simulated
892 alignment contained 208 chromosomes and we kept only coalescent simulations that contained \leq

893 5,000 segregating sites, and again padded with zeros so that all matrices were 208×5000 . This
894 left 238,655 simulations, and from those we constructed a training set of 233,655 simulations. In
895 trial runs, we found that regions flanking hard and soft sweeps were the most difficult classes to
896 predict, so we again simulated additional examples from these more challenging classes. This
897 shifted the balance of our training set so that it was comprised of approximately 13% neutral
898 regions, 17% each for hard and soft sweeps, and 26.5% each for regions linked to nearby hard
899 and soft sweeps windows. We then set aside an evenly balanced set of 2,000 simulations for
900 validation and 3,000 for testing.

901 As before, we sorted each matrix by genetic similarity among chromosomes and then
902 transposed the matrix to 5000×208 . We also extracted the segregating site positions vector from
903 these simulations which were generated by **discoal** (Kern and Schrider 2016), which like **ms**
904 represents each position as a real number between zero and one.

905 As above, we trained a CNN with two input branches. The first branch took the
906 haplotype matrices as input and included five 1D-convolutional layers (kernel size = 2), each
907 followed by average-pooling. These layers each contained 256 neurons and used dropout
908 normalization (20%). The second branch took the position vector as input and contained one
909 densely connected layer with 64 neurons, again using dropout normalization (10%). The two
910 branches were then merged into another densely connected layer of 256 neurons with 25%
911 dropout. Each hidden layer of the network used L2-regularization of the weights ($\lambda = 0.0001$)
912 and ReLU as the activation function. Finally, the output of this layer was fed to a five neuron
913 layer with softmax activation functions that predicts the five classes given above. The CNN was
914 trained using the Adam optimization algorithm, the categorical cross-entropy loss function, and a
915 mini-batch size of 32. The CNN was trained for 3 iterations.

916

917 **Inferring population size histories**

918 To show how CNNs can be used to infer species' demographic histories, and how CNN
919 architecture can impact this inference, we experimented with a variety of CNN approaches to
920 infer the 5 parameters of a 3-epoch model of instantaneous population size changes (i.e. 3
921 population sizes and 2 times of size change). We also use this challenging problem as an
922 opportunity to evaluate how alternative approaches to building a CNN can influence its
923 performance. In effect, we conducted a full grid search of the following attributes of both our

924 CNN architecture and input/output format: the dimensionality of our convolutions (1D or 2D),
925 the kernel size (i.e. the width of our 1D convolutional filters and both the height and width of our
926 square 2D filters; we tried each multiple of 2 ranging from 2 to 10), whether to include dropout
927 (yes or no) following max pooling steps or dense layers, whether to sort our rows based on
928 similarity (yes or no), whether to log-scale our response variables (yes or no), and whether to
929 represent ancestral and derived alleles as -1/1 or as 0/255. When included, our dropout layers
930 immediately followed both max pooling steps, the dense layer following the distance input layer,
931 and the final dense layer. Each of these dropout steps randomly removed 25% of neurons. Each
932 response variable was transformed to a \tilde{z} -score according to the sample mean and variance for
933 that variable across all simulated examples.

934 The network we used for this task had two branches: a standard CNN like that depicted
935 in Fig. 1B–C but with more convolutional layers (four CNN layers each producing 128 filters and
936 each followed by a max pooling layer with a kernel size of 2), and a dense neural network layer
937 (consisting of 32 nodes) taking positional information as its input, and concatenating its output
938 with that of the final max pooling layer of the CNN prior to being fed into the final dense layer
939 (256 nodes). The positional information was a vector, \mathbf{d} , whose length was the maximum of the
940 number of segregating sites observed across all simulated examples minus one. Each value in the
941 vector d_i was simply the distance (scaled between zero and one where one is the total length of the
942 simulated region) between segregating site i and site $i-1$.

943 In total, we simulated 100,000 alignments of phased chromosomes using `ms`. 10,000 each
944 were set aside for testing and validation, while the remaining 80,000 were used for training. The
945 simulated population size histories were generated randomly—each demographic model
946 parameter was drawn uniformly from a range listed in supplementary table S2. Each simulated
947 region was roughly equivalent 1.5 Mbp in the human genome, assuming per base pair mutation
948 and recombination rates of 1.2×10^{-8} and 1×10^{-8} , respectively. However, in order to make the size
949 of the simulation output more tractable for processing in a CNN we divided the mutation rate by
950 10 (equivalent to randomly downsampling the number of polymorphisms included in the input
951 by a factor of 10). During training we used a batch size of 200, trained our networks for up to 10
952 iterations, and retained the best performing CNN as assessed on the validation set. Often the best
953 CNN was obtained prior to completing all 10 training iterations. We then evaluated the
954 performance of the best CNN for each network architecture and input format on the test set by

955 calculating total RMSE (our loss function for this task); we also calculated Spearman correlation
956 coefficients between the true and predicted values for each of the five demographic model
957 parameters.

958

959 **ACKNOWLEDGMENTS**

960 We thank Matt Hahn for comments on the manuscript. DRS was funded by the National
961 Institutes of Health under award number R00HG008696. YB would like to acknowledge the
962 Minnesota Supercomputing Institute for computational resources.

963

964 **REFERENCES**

- 965 Arnold, B., K. Bomblies and J. Wakeley, 2012 Extending coalescent theory to autotetraploids.
966 *Genetics* **192**: 195-204.
- 967 Auton, A., L. D. Brooks, R. M. Durbin, E. P. Garrison, H. M. Kang *et al.*, 2015 A global
968 reference for human genetic variation. *Nature* **526**: 68-74.
- 969 Auton, A., and G. McVean, 2007 Recombination rate estimation in the presence of hotspots.
970 *Genome Res.* **17**: 1219-1227.
- 971 Beaumont, M. A., 2010 Approximate Bayesian computation in evolution and ecology. *Annual*
972 *review of ecology, evolution, and systematics* **41**: 379-406.
- 973 Begun, D. J., and C. F. Aquadro, 1992 Levels of naturally occurring DNA polymorphism
974 correlate with recombination rates in *D. melanogaster*. *Nature* **356**: 519-520.
- 975 Begun, D. J., A. K. Holloway, K. Stevens, L. W. Hillier, Y.-P. Poh *et al.*, 2007 Population
976 genomics: whole-genome analysis of polymorphism and divergence in *Drosophila*
977 *simulans*. *PLoS Biol.* **5**: e310.
- 978 Bellot, P., G. de los Campos and M. Pérez-Enciso, 2018 Can Deep Learning Improve Genomic
979 Prediction of Complex Human Traits? *Genetics*: genetics. 301298.302018.
- 980 Boitard, S., C. Schlötterer and A. Futschik, 2009 Detecting selective sweeps: a new approach
981 based on hidden Markov models. *Genetics* **181**: 1567-1578.
- 982 Brandvain, Y., A. M. Kenney, L. Flagel, G. Coop and A. L. Sweigart, 2014 Speciation and
983 introgression between *Mimulus nasutus* and *Mimulus guttatus*. *PLoS Genet.* **10**: e1004410.
- 984 Breiman, L., 2001 Statistical modeling: The two cultures (with comments and a rejoinder by the
985 author). *Statistical science* **16**: 199-231.
- 986 Chan, A. H., P. A. Jenkins and Y. S. Song, 2012 Genome-wide fine-scale recombination rate
987 variation in *Drosophila melanogaster*. *PLoS Genet.* **8**: e1003090.
- 988 Chan, J., V. Perrone, J. P. Spence, P. A. Jenkins, S. Mathieson *et al.*, 2018 A Likelihood-Free
989 Inference Framework for Population Genetic Data using Exchangeable Neural Networks.
990 *bioRxiv*.
- 991 Charlesworth, B., M. Morgan and D. Charlesworth, 1993 The effect of deleterious mutations on
992 neutral molecular variation. *Genetics* **134**: 1289-1303.
- 993 Chilimbi, T. M., Y. Suzue, J. Apacible and K. Kalyanaraman, 2014 Project Adam: Building an
994 Efficient and Scalable Deep Learning Training System, pp. 571-582 in *OSDI*.

- 995 Corbett-Detig, R., and R. Nielsen, 2017 A hidden Markov model approach for simultaneously
996 estimating local ancestry and admixture time using next generation sequence data in
997 samples of arbitrary ploidy. *PLoS Genet.* **13**: e1006529.
- 998 Dieleman, S., and B. Schrauwen, 2014 End-to-end learning for music audio, pp. 6964-6968 in
999 *Acoustics, Speech and Signal Processing (ICASSP), 2014 IEEE International Conference on.* IEEE.
- 1000 Dutheil, J. Y., G. Ganapathy, A. Hobolth, T. Mailund, M. K. Uyenoyama *et al.*, 2009 Ancestral
1001 population genomics: the coalescent hidden Markov model approach. *Genetics* **183**: 259-
1002 274.
- 1003 Elyashiv, E., S. Sattath, T. T. Hu, A. Strutsosky, G. McVicker *et al.*, 2016 A genomic map of
1004 the effects of linked selection in *Drosophila*. *PLoS Genet.* **12**: e1006130.
- 1005 Ewing, G., and J. Hermisson, 2010 MSMS: a coalescent simulation program including
1006 recombination, demographic structure and selection at a single locus. *Bioinformatics* **26**:
1007 2064-2065.
- 1008 Fay, J. C., and C.-I. Wu, 2000 Hitchhiking under positive Darwinian selection. *Genetics* **155**:
1009 1405-1413.
- 1010 Ferrer-Admetlla, A., M. Liang, T. Korneliussen and R. Nielsen, 2014 On detecting incomplete
1011 soft or hard selective sweeps using haplotype structure. *Mol. Biol. Evol.* **31**: 1275-1291.
- 1012 Fontaine, M. C., J. B. Pease, A. Steele, R. M. Waterhouse, D. E. Neafsey *et al.*, 2015 Extensive
1013 introgression in a malaria vector species complex revealed by phylogenomics. *Science* **347**:
1014 1258524.
- 1015 Fu, Y.-X., and W.-H. Li, 1993 Statistical tests of neutrality of mutations. *Genetics* **133**: 693-709.
- 1016 Gao, F., C. Ming, W. Hu and H. Li, 2016 New software for the fast estimation of population
1017 recombination rates (FastEPRR) in the genomic era. *G3: Genes, Genomes, Genetics* **6**: 1563-
1018 1571.
- 1019 Garrigan, D., S. B. Kingan, A. J. Geneva, P. Andolfatto, A. G. Clark *et al.*, 2012 Genome
1020 sequencing reveals complex speciation in the *Drosophila simulans* clade. *Genome Res.* **22**:
1021 1499-1511.
- 1022 Garud, N. R., P. W. Messer, E. O. Buzbas and D. A. Petrov, 2015 Recent selective sweeps in
1023 North American *Drosophila melanogaster* show signatures of soft sweeps. *PLoS Genet.* **11**:
1024 e1005004.
- 1025 Gazave, E., L. Ma, D. Chang, A. Coventry, F. Gao *et al.*, 2014 Neutral genomic regions refine
1026 models of recent rapid human population growth. *Proceedings of the National Academy of*
1027 *Sciences* **111**: 757-762.
- 1028 Geneva, A. J., C. A. Muirhead, S. B. Kingan and D. Garrigan, 2015 A new method to scan
1029 genomes for introgression in a secondary contact model. *PLoS ONE* **10**: e0118621.
- 1030 Gutenkunst, R. N., R. D. Hernandez, S. H. Williamson and C. D. Bustamante, 2009 Inferring
1031 the joint demographic history of multiple populations from multidimensional SNP
1032 frequency data. *PLoS Genet.* **5**: e1000695.
- 1033 Hahn, M. W., 2018 *Molecular Population Genetics*. Oxford University Press.
- 1034 Hahnloser, R. H., R. Sarpeshkar, M. A. Mahowald, R. J. Douglas and H. S. Seung, 2000 Digital
1035 selection and analogue amplification coexist in a cortex-inspired silicon circuit. *Nature*
1036 **405**: 947.
- 1037 Haller, B., and P. Messer, 2017 SLiM 2: Flexible, Interactive Forward Genetic Simulations. *Mol.*
1038 *Biol. Evol.* **34**: 230.
- 1039 Hedrick, P. W., 2013 Adaptive introgression in animals: examples and comparison to new
1040 mutation and standing variation as sources of adaptive variation. *Mol. Ecol.* **22**: 4606-
1041 4618.

- 1042 Hellenthal, G., G. B. Busby, G. Band, J. F. Wilson, C. Capelli *et al.*, 2014 A genetic atlas of
1043 human admixture history. *Science* **343**: 747-751.
- 1044 Hermisson, J., and P. S. Pennings, 2005 Soft sweeps molecular population genetics of adaptation
1045 from standing genetic variation. *Genetics* **169**: 2335-2352.
- 1046 Hey, J., 2009 Isolation with migration models for more than two populations. *Mol. Biol. Evol.* **27**:
1047 905-920.
- 1048 Hey, J., and J. Wakeley, 1997 A coalescent estimator of the population recombination rate.
1049 *Genetics* **145**: 833-846.
- 1050 Hill, W. G., and A. Robertson, 1966 The effect of linkage on limits to artificial selection. *Genetics*
1051 *Research* **8**: 269-294.
- 1052 Hobolth, A., O. F. Christensen, T. Mailund and M. H. Schierup, 2007 Genomic relationships
1053 and speciation times of human, chimpanzee, and gorilla inferred from a coalescent
1054 hidden Markov model. *PLoS Genet.* **3**: e7.
- 1055 Hornik, K., 1991 Approximation capabilities of multilayer feedforward networks. *Neural networks*
1056 **4**: 251-257.
- 1057 Hudson, R. R., 1987 Estimating the recombination parameter of a finite population model
1058 without selection. *Genetics Research* **50**: 245-250.
- 1059 Hudson, R. R., 2001 Two-locus sampling distributions and their application. *Genetics* **159**: 1805-
1060 1817.
- 1061 Hudson, R. R., 2002 Generating samples under a Wright–Fisher neutral model of genetic
1062 variation. *Bioinformatics* **18**: 337-338.
- 1063 Hudson, R. R., and N. L. Kaplan, 1985 Statistical properties of the number of recombination
1064 events in the history of a sample of DNA sequences. *Genetics* **111**: 147-164.
- 1065 Jensen, J. D., Y. Kim, V. B. DuMont, C. F. Aquadro and C. D. Bustamante, 2005
1066 Distinguishing between selective sweeps and demography using DNA polymorphism
1067 data. *Genetics* **170**: 1401-1410.
- 1068 Joly, S., P. A. McLenachan and P. J. Lockhart, 2009 A statistical approach for distinguishing
1069 hybridization and incomplete lineage sorting. *The American Naturalist* **174**: E54-E70.
- 1070 Jouppi, N. P., C. Young, N. Patil, D. Patterson, G. Agrawal *et al.*, 2017 In-datacenter
1071 performance analysis of a tensor processing unit, pp. 1-12 in *Proceedings of the 44th Annual*
1072 *International Symposium on Computer Architecture*. ACM.
- 1073 Kaplan, N. L., R. Hudson and C. Langley, 1989 The "hitchhiking effect" revisited. *Genetics* **123**:
1074 887-899.
- 1075 Kelleher, J., A. M. Etheridge and G. McVean, 2016 Efficient coalescent simulation and
1076 genealogical analysis for large sample sizes. *PLoS Comput. Biol.* **12**: e1004842.
- 1077 Kelleher, J., K. Thornton, J. Ashander and P. Ralph, 2018 Efficient pedigree recording for fast
1078 population genetics simulation. *bioRxiv*: 248500.
- 1079 Kelly, J. K., 1997 A test of neutrality based on interlocus associations. *Genetics* **146**: 1197-1206.
- 1080 Kern, A. D., and D. Haussler, 2010 A population genetic hidden Markov model for detecting
1081 genomic regions under selection. *Mol. Biol. Evol.* **27**: 1673-1685.
- 1082 Kern, A. D., and D. R. Schrider, 2016 discoal: flexible coalescent simulations with selection.
1083 *Bioinformatics* **32**: btw556.
- 1084 Kim, Y., 2014 Convolutional neural networks for sentence classification. *arXiv preprint*
1085 *arXiv:1408.5882*.
- 1086 Kim, Y., and R. Nielsen, 2004 Linkage disequilibrium as a signature of selective sweeps. *Genetics*
1087 **167**: 1513-1524.

- 1088 Kim, Y., and W. Stephan, 2002 Detecting a local signature of genetic hitchhiking along a
1089 recombining chromosome. *Genetics* **160**: 765-777.
- 1090 Kingma, D. P., and J. Ba, 2014 Adam: A method for stochastic optimization. *arXiv preprint*
1091 *arXiv:1412.6980*.
- 1092 Kong, A., G. Thorleifsson, D. F. Gudbjartsson, G. Masson, A. Sigurdsson *et al.*, 2010 Fine-scale
1093 recombination rate differences between sexes, populations and individuals. *Nature* **467**:
1094 1099-1103.
- 1095 Korneliussen, T. S., A. Albrechtsen and R. Nielsen, 2014 ANGSD: analysis of next generation
1096 sequencing data. *BMC Bioinformatics* **15**: 356.
- 1097 Köster, U., T. Webb, X. Wang, M. Nassar, A. K. Bansal *et al.*, 2017 Flexpoint: An adaptive
1098 numerical format for efficient training of deep neural networks, pp. 1742-1752 in *Advances*
1099 *in Neural Information Processing Systems*.
- 1100 Krizhevsky, A., I. Sutskever and G. E. Hinton, 2012 Imagenet classification with deep
1101 convolutional neural networks, pp. 1097-1105 in *Advances in neural information processing*
1102 *systems*.
- 1103 Kulathinal, R. J., L. S. Stevison and M. A. Noor, 2009 The genomics of speciation in
1104 *Drosophila*: diversity, divergence, and introgression estimated using low-coverage
1105 genome sequencing. *PLoS Genet.* **5**: e1000550.
- 1106 Langley, C. H., K. Stevens, C. Cardeno, Y. C. G. Lee, D. R. Schrider *et al.*, 2012 Genomic
1107 variation in natural populations of *Drosophila melanogaster*. *Genetics* **192**: 533-598.
- 1108 Lawrence, S., C. L. Giles, A. C. Tsoi and A. D. Back, 1997 Face recognition: A convolutional
1109 neural-network approach. *IEEE transactions on neural networks* **8**: 98-113.
- 1110 Lawson, D. J., G. Hellenthal, S. Myers and D. Falush, 2012 Inference of population structure
1111 using dense haplotype data. *PLoS Genet.* **8**: e1002453.
- 1112 LeCun, Y., Y. Bengio and G. Hinton, 2015 Deep learning. *Nature* **521**: 436-444.
- 1113 LeCun, Y., L. Bottou, Y. Bengio and P. Haffner, 1998 Gradient-based learning applied to
1114 document recognition. *Proceedings of the IEEE* **86**: 2278-2324.
- 1115 Li, H., and R. Durbin, 2011 Inference of human population history from individual whole-
1116 genome sequences. *Nature* **475**: 493-496.
- 1117 Li, N., and M. Stephens, 2003 Modeling linkage disequilibrium and identifying recombination
1118 hotspots using single-nucleotide polymorphism data. *Genetics* **165**: 2213-2233.
- 1119 Lin, K., A. Futschik and H. Li, 2013 A fast estimate for the population recombination rate based
1120 on regression. *Genetics* **194**: 473-484.
- 1121 Lin, K., H. Li, C. Schlötterer and A. Futschik, 2011 Distinguishing positive selection from
1122 neutral evolution: boosting the performance of summary statistics. *Genetics* **187**: 229-244.
- 1123 Lipson, M., P.-R. Loh, A. Levin, D. Reich, N. Patterson *et al.*, 2013 Efficient moment-based
1124 inference of admixture parameters and sources of gene flow. *Mol. Biol. Evol.* **30**: 1788-
1125 1802.
- 1126 Liu, X., and Y.-X. Fu, 2015 Exploring population size changes using SNP frequency spectra.
1127 *Nat. Genet.* **47**: 555-559.
- 1128 Loh, P.-R., M. Lipson, N. Patterson, P. Moorjani, J. K. Pickrell *et al.*, 2013 Inferring admixture
1129 histories of human populations using linkage disequilibrium. *Genetics* **193**: 1233-1254.
- 1130 Lu, X., Z. Lin, X. Shen, R. Mech and J. Z. Wang, 2015 Deep multi-patch aggregation network
1131 for image style, aesthetics, and quality estimation, pp. 990-998 in *Proceedings of the IEEE*
1132 *International Conference on Computer Vision*.

- 1133 Marth, G. T., E. Czabarka, J. Murvai and S. T. Sherry, 2004 The allele frequency spectrum in
1134 genome-wide human variation data reveals signals of differential demographic history in
1135 three large world populations. *Genetics* **166**: 351-372.
- 1136 Martin, S. H., K. K. Dasmahapatra, N. J. Nadeau, C. Salazar, J. R. Walters *et al.*, 2013
1137 Genome-wide evidence for speciation with gene flow in *Heliconius* butterflies. *Genome Res.*
1138 **23**: 1817-1828.
- 1139 Maynard Smith, J., and J. Haigh, 1974 The hitch-hiking effect of a favourable gene. *Genet. Res.*
1140 **23**: 23-35.
- 1141 McVean, G. A., S. R. Myers, S. Hunt, P. Deloukas, D. R. Bentley *et al.*, 2004 The fine-scale
1142 structure of recombination rate variation in the human genome. *Science* **304**: 581-584.
- 1143 Mitchell, T. M., 1997 Artificial neural networks. *Machine Learning* **45**: 81-127.
- 1144 Nair, V., and G. E. Hinton, 2010 Rectified linear units improve restricted boltzmann machines,
1145 pp. 807-814 in *Proceedings of the 27th international conference on machine learning (ICML-10)*.
- 1146 Nielsen, R., and J. Wakeley, 2001 Distinguishing migration from isolation: a Markov chain
1147 Monte Carlo approach. *Genetics* **158**: 885-896.
- 1148 Nielsen, R., S. Williamson, Y. Kim, M. J. Hubisz, A. G. Clark *et al.*, 2005 Genomic scans for
1149 selective sweeps using SNP data. *Genome Res.* **15**: 1566-1575.
- 1150 Pavlidis, P., J. D. Jensen and W. Stephan, 2010 Searching for footprints of positive selection in
1151 whole-genome SNP data from nonequilibrium populations. *Genetics* **185**: 907-922.
- 1152 Price, A. L., A. Tandon, N. Patterson, K. C. Barnes, N. Rafaels *et al.*, 2009 Sensitive detection of
1153 chromosomal segments of distinct ancestry in admixed populations. *PLoS Genet.* **5**:
1154 e1000519.
- 1155 Pudlo, P., J.-M. Marin, A. Estoup, J.-M. Cornuet, M. Gautier *et al.*, 2016 Reliable ABC model
1156 choice via random forests. *Bioinformatics* **32**: 859-866.
- 1157 Pybus, M., P. Luisi, G. M. Dall'Olio, M. Uzkudun, H. Laayouni *et al.*, 2015 Hierarchical
1158 boosting: a machine-learning framework to detect and classify hard selective sweeps in
1159 human populations. *Bioinformatics* **31**: 3946-3952.
- 1160 Racimo, F., D. Marnetto and E. Huerta-Sanchez, 2016 Signatures of archaic adaptive
1161 introgression in present-day human populations. *Mol. Biol. Evol.* **34**: 296-317.
- 1162 Rasmussen, M. D., M. J. Hubisz, I. Gronau and A. Siepel, 2014 Genome-wide inference of
1163 ancestral recombination graphs.
- 1164 Ribeiro, M. T., S. Singh and C. Guestrin, 2016 Why should i trust you?: Explaining the
1165 predictions of any classifier, pp. 1135-1144 in *Proceedings of the 22nd ACM SIGKDD*
1166 *International Conference on Knowledge Discovery and Data Mining*. ACM.
- 1167 Ronen, R., N. Udpa, E. Halperin and V. Bafna, 2013 Learning natural selection from the site
1168 frequency spectrum. *Genetics* **195**: 181-193.
- 1169 Rosenzweig, B. K., J. B. Pease, N. J. Besansky and M. W. Hahn, 2016 Powerful methods for
1170 detecting introgressed regions from population genomic data. *Mol. Ecol.* **25**: 2387-2397.
- 1171 Rumelhart, D. E., G. E. Hinton and R. J. Williams, 1986 Learning representations by back-
1172 propagating errors. *Nature* **323**: 533.
- 1173 Sankararaman, S., S. Mallick, M. Dannemann, K. Prüfer, J. Kelso *et al.*, 2014 The genomic
1174 landscape of Neanderthal ancestry in present-day humans. *Nature* **507**: 354-357.
- 1175 Schiffels, S., and R. Durbin, 2014 Inferring human population size and separation history from
1176 multiple genome sequences. *Nat. Genet.* **46**: 919-925.
- 1177 Schlötterer, C., R. Tobler, R. Kofler and V. Nolte, 2014 Sequencing pools of individuals—
1178 mining genome-wide polymorphism data without big funding. *Nature Reviews Genetics* **15**:
1179 749.

- 1180 Schrider, D., J. Ayroles, D. R. Matute and A. D. Kern, 2018 Supervised machine learning
1181 reveals introgressed loci in the genomes of *Drosophila simulans* and *D. sechellia*. *PLoS Genet.*
1182 **14**: e1007341.
- 1183 Schrider, D. R., and A. D. Kern, 2015 Inferring selective constraint from population genomic
1184 data suggests recent regulatory turnover in the human brain. *Genome Biol. Evol.* **7**: 3511-
1185 3528.
- 1186 Schrider, D. R., and A. D. Kern, 2016 S/HIC: Robust Identification of Soft and Hard Sweeps
1187 Using Machine Learning. *PLoS Genet.* **12**: e1005928.
- 1188 Schrider, D. R., and A. D. Kern, 2017 Soft sweeps are the dominant mode of adaptation in the
1189 human genome. *Mol. Biol. Evol.* **34**: 1863–1877.
- 1190 Schrider, D. R., and A. D. Kern, 2018 Supervised Machine Learning for Population Genetics: A
1191 New Paradigm. *Trends Genet.* **34**: 301-312.
- 1192 Schrider, D. R., F. K. Mendes, M. W. Hahn and A. D. Kern, 2015 Soft shoulders ahead:
1193 spurious signatures of soft and partial selective sweeps result from linked hard sweeps.
1194 *Genetics* **200**: 267-284.
- 1195 Sheehan, S., and Y. S. Song, 2016 Deep learning for population genetic inference. *PLoS Comput.*
1196 *Biol.* **12**: e1004845.
- 1197 Simonsen, K. L., G. A. Churchill and C. F. Aquadro, 1995 Properties of statistical tests of
1198 neutrality for DNA polymorphism data. *Genetics* **141**: 413-429.
- 1199 Simonyan, K., and A. Zisserman, 2014 Very deep convolutional networks for large-scale image
1200 recognition. *arXiv preprint arXiv:1409.1556*.
- 1201 Smith, J., G. Coop, M. Stephens and J. Novembre, 2018 Estimating time to the common
1202 ancestor for a beneficial allele. *Mol. Biol. Evol.*
- 1203 Snoek, J., H. Larochelle and R. P. Adams, 2012 Practical bayesian optimization of machine
1204 learning algorithms, pp. 2951-2959 in *Advances in neural information processing systems*.
- 1205 Sohn, K.-A., Z. Ghahramani and E. P. Xing, 2012 Robust estimation of local genetic ancestry in
1206 admixed populations using a nonparametric Bayesian approach. *Genetics* **191**: 1295-1308.
- 1207 Srivastava, N., G. Hinton, A. Krizhevsky, I. Sutskever and R. Salakhutdinov, 2014 Dropout: A
1208 simple way to prevent neural networks from overfitting. *The Journal of Machine Learning*
1209 *Research* **15**: 1929-1958.
- 1210 Sugden, L. A., E. G. Atkinson, A. P. Fischer, S. Rong, B. M. Henn *et al.*, 2018 Localization of
1211 adaptive variants in human genomes using averaged one-dependence estimation. *Nature*
1212 *Communications* **9**: 703.
- 1213 Szegedy, C., W. Liu, Y. Jia, P. Sermanet, S. Reed *et al.*, 2015 Going deeper with convolutions,
1214 pp. in *CVPR*.
- 1215 Tajima, F., 1989 Statistical method for testing the neutral mutation hypothesis by DNA
1216 polymorphism. *Genetics* **123**: 585-595.
- 1217 Tennessen, J. A., A. W. Bigham, T. D. O'Connor, W. Fu, E. E. Kenny *et al.*, 2012 Evolution and
1218 functional impact of rare coding variation from deep sequencing of human exomes.
1219 *Science* **337**: 64-69.
- 1220 Teshima, K. M., and H. Innan, 2009 mbs: modifying Hudson's ms software to generate samples
1221 of DNA sequences with a biallelic site under selection. *BMC Bioinformatics* **10**: 166.
- 1222 Thornton, K. R., 2014 A C++ template library for efficient forward-time population genetic
1223 simulation of large populations. *Genetics* **198**: 157-166.
- 1224 Turner, T. L., M. W. Hahn and S. V. Nuzhdin, 2005 Genomic islands of speciation in
1225 *Anopheles gambiae*. *PLoS Biol.* **3**: e285.

- 1226 Voight, B. F., S. Kudaravalli, X. Wen and J. K. Pritchard, 2006 A map of recent positive
1227 selection in the human genome. *PLoS Biol.* **4**: e72.
- 1228 Vy, H. M. T., and Y. Kim, 2015 A Composite-Likelihood Method for Detecting Incomplete
1229 Selective Sweep from Population Genomic Data. *Genetics* **200**: 633-649.
- 1230 Washburn, J. D., M. K. M. Guerra, G. Ramstein, K. A. Kremling, R. Valluru *et al.*, 2018
1231 Evolutionarily informed deep learning methods: Predicting transcript abundance from
1232 DNA sequence. *bioRxiv*: 372367.
- 1233 Yu, F., and V. Koltun, 2015 Multi-scale context aggregation by dilated convolutions. *arXiv*
1234 *preprint arXiv:1511.07122*.
- 1235 Zaheer, M., S. Kottur, S. Ravanbakhsh, B. Póczos, R. R. Salakhutdinov *et al.*, 2017 Deep sets,
1236 pp. 3394-3404 in *Advances in Neural Information Processing Systems*.
- 1237

1238

1239 **SUPPLEMENTARY TABLE LEGENDS**

1240

1241 **Supplementary table S1: The effect of different neural network**
1242 **input/output/architecture hyperparameters on demographic inference error.**

1243

1244 **Supplementary table S2: Demographic parameter ranges used to simulate 3-epoch**
1245 **population size histories.**